1-1-2012

Origin of surface undulations at the Kamb Ice Stream grounding line, West Antarctica

Fiona Bronwyn Seifert
Portland State University

Origin of surface undulations at the Kamb Ice Stream grounding line, West Antarctica

by

Fiona Bronwyn Seifert

A thesis submitted in partial fulfillment of the
requirements for the degree of

Master of Science
in
Geology

Thesis Committee:
Christina Hulbe, Chair
Kenneth Cruickshank
Andrew Fountain

Portland State University

Abstract

The West Antarctic Ice Sheet is drained primarily by five major ice streams, which together control the volume of ice discharged into the ocean across the grounding line. The grounding line of Kamb Ice Stream (KIS) is unusual because the ice stream upstream of it is stagnant. Here, a set of surface features--shore-parallel, long wavelength, low amplitude undulations--found only at that grounding line are examined and found to be "pinch and swell" features formed by an instability in the viscous deformation of the ice. When a relatively competent layer is surrounded by lower strength materials, particular wavelength features within the layer may be amplified under certain layer thickness and strain rate conditions. The undulations at KIS grounding line are possible due to the relatively large strain rates and particular ice thickness at that location.

Several data sets are used to characterize the surface features. High resolution surface profiles are created using kinematic GPS carried on board a sled that was used to tow ice penetrating radar equipment. The radar data are used to examine the relationship between surface shape and basal crevasses. Additional surface profiles are created using ICESat laser altimeter observations. Repeat GPS surveys of a strain grid across the grounding line yields strain rate information. Analysis of repeat observations over tidal cycles and multi-day intervals shows that the features are not standing or traveling waves. Together, these observations

are then used to evaluate the contributions of elastic and viscous deformation of the ice in creating the grounding line undulations.

Dedication

I would like to dedicate this work to my family; those alive and those who have passed.

Acknowledgements

First, I would like to thank my family whose endless support and encouragement allowed me to follow my dreams and become who I am today. I have had the privilege of interacting with so many faculty members, students, and friends throughout my education who have enriched my education and consequently my life. You have made my education a joy.

During my second year of college, I stumbled upon a class on geology that fulfilled my science requirement. I expected the course to be just like any other general requirement, interesting at times but ultimately just a step towards another goal. What I found was an amazing instructor who invited me into a world that explored our planet and I was hooked. Charlene Montierth if you had not been the instructor you are I may not have ever discovered the science I have come to love so much, thank you.

The Portland State University Geology Department is composed of incredible people whose enthusiasm is inspiring. It was a privilege to be your student, colleague, and friend. I would also like to take this opportunity to thank those members of the glaciological community who have taken the time to talk to me about my research, ask questions, and ultimately help me to become a better scientist.

I would like to thank my committee for their guidance, time, and support. Your advice was and is always appreciated. And last, I would like to thank my

advisor Christina Hulbe without whom this research would not have been possible. Christina has continuously challenged me, supported me, and inspired me. Under her guidance my skills as a scientist have been honed into tools that I can use to explore the world. This is a gift I will always remember, thank you.

Table of Contents

List of Figures

Symbol Guide

Latin letters (Upper case)

A	amplitude of the undulation		m
A_o	amplitude of slope approaching grounding line		m
C	creep parameter		
D	flexural rigidity		Pa m^3
E	elastic modulus	9 x 10^9	Pa
I	area moment of inertia		
L	length of the beam		m
$M(x)$	bending moment of an elastic beam		
$\tilde{P}$	pressure		

Latin letters (lower case)

d	mean thickness of ice, not including		m
g	force due to gravity	9.8	m s^{-2}
h	ice thickness		m
k	wave number		unitless
k_0	stiffness coefficient	9114	kg m^{-2} s^{-2}
l	bending length scale		m
q	load on the elastic beam		Pa
u, v	velocity vectors for $[x, y]$		m a^{-1}
u_b, v_b	velocity components for the centroid of a triangle		m a^{-1}
v	Poisson's ratio	.314	unitless
$\bar{v}_x$	mean velocity in the x direction		m s^{-1}
$\bar{v}_z$	mean velocity in the z direction		m s^{-1}
$\Delta x_i, \Delta y_i$	distance from any vertex of the triangle to the centroid		m
w_a	unbent position of the beam		m
$w(x)$	deflection of the beam with respect to x		m
x_b	x coordinate for a triangular centroid		m
y_b	y coordinate for a triangular centroid		m

Greek letters

β	damping factor		m^{-1}
$\dot{\epsilon}$	strain rate tensor		a^{-1}
$\dot{\epsilon}_{jk}$	strain rate		a^{-1}
λ	wavelength		km
μ_n	viscosity in the normal direction		Pa s
μ_s	viscosity in the shear direction		Pa s
ρ_i	density of ice	910	kg m^{-3}
ρ_{sw}	density of seawater	1025	kg m^{-3}
τ_{jk}	deviatoric stress		Pa
ψ	stream function		
$\bar{\psi}$	primary flow		
$\tilde{\psi}$	perturbed flow		

1 Introduction

Marine ice sheets are defined by three characteristics: the subglacial bed is below sea level, the bed is in some locations mantled by unconsolidated marine clay, and the ice is in contact with the ocean at its downstream margin (Figure 1) (Alley and Bindschadler, 2001; Mercer, 1978; Schoof, 2007; Weertman, 1974). The ice mass accumulates as snow falls on the ice sheet surface and flows from the interior of the ice sheet towards the margins, where ice is lost to iceberg calving, melting, and sublimation. Where the bed consists of marine clay, the low strength and high pore water pressure of the subglacial material (till) provide little resistance and as a result ice moves rapidly downstream towards the ocean in features called ice streams (Kamb, 2001). Ice streams are separated by slow-flowing interstream ridges, where the bed is relatively high and liquid water is not abundant at the ice/bed interface (Whillans et al., 2001). Along much of the coastal margin, ice goes afloat to form embayment-filling ice shelves. The transition between grounded inland ice and the floating shelf is called the grounding line, or grounding zone. At some locations, the transition from the grounded to floating ice is distinct forming a grounding line. In other places, the transition occurs over a plain that is usually a few km's wide and considered a grounding zone (Fricker and Padman, 2006). Ice in the grounding zone is close to floating allowing it to fluctuate between grounded and floating with changes to sea level such as tidal fluctuations.

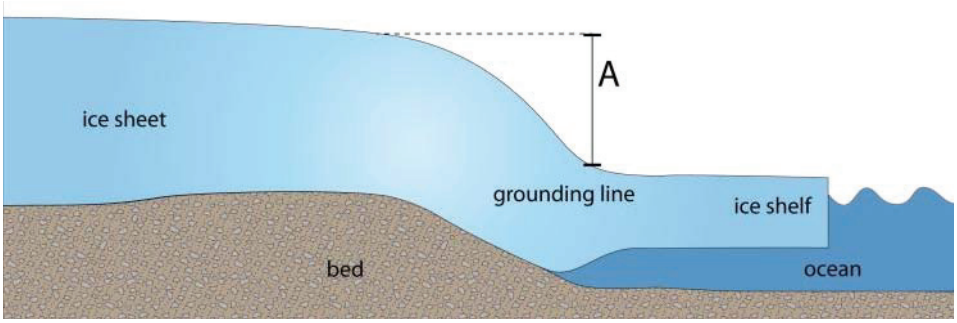

Figure 1: Cartoon of transition of grounded to floating ice.

The location of the grounding line or zone depends on both the flow of the ice sheet and the ice shelf into which it discharges. When ice begins to float at an ice stream grounding line, the resistive stress at its base goes from small to zero, the rate at which the ice flows increases, and the local thinning rate increases relative to the thinning rate upstream. If the thinning rate increases enough to cause ice upstream of the grounding line to float, the upstream ice will speed up and thin as well. Where the bed deepens toward the interior, the retreat may continue for some distance upstream. The role of the ice shelf is to modify the stress balance at the grounding line, an effect that depends on the geometry of the shelf itself (Schoof, 2007). If the geometry of the shelf changes (perhaps due to a change in melting or iceberg calving), so too will the location of the grounding line.

Ice at the grounding line is influenced by the ocean. The surface height of the ice shelf changes continuously with the tide, which in turn changes the slope of the grounding line transition and the angle of flexure. This interaction with the ocean causes continuous perturbations to the stress field within the ice as the ice shelf moves through the tide cycle. These perturbations can be seen 100's of ice

thicknesses upstream or downstream, out onto the floating ice shelf as a seismic wave (Anandakrishnan and Alley, 1997).

1.1 The West Antarctic Ice-sheet and Kamb Ice Stream

The West Antarctic Ice-sheet (WAIS) is a marine ice sheet. Most of the mass flux out of the Ross Sea sector of the West Antarctic Ice-sheet (WAIS) discharges through five relatively fast flowing ice streams (Figure 2) (Bindschadler et al., 2001; Shabtaie and Bentley, 1987). Kamb Ice Stream (KIS) is one of the major outlets from the WAIS into the Ross Ice Shelf (RIS) (Figure 2). The ice stream is bounded by Siple Dome (SD) to the north and Engelhart Ridge (ER) to the south. KIS is different from other ice streams draining into the WAIS due to its stagnate nature which leads to unusual flows features downstream of the grounding line

KIS ceased its rapid flow about 150 years ago, but, prior to that time, experienced flow speeds similar to adjacent ice streams (Catania et al., 2006; Ng and Conway, 2004; Retzlaff and Bentley, 1993). The kinematic state at KIS grounding line is unlike that of any of the other Ross ice streams. In all cases, the basal boundary condition changes abruptly where the ice goes afloat (basal traction is non-zero upstream and zero downstream of the groundling line) but at KIS, the basal traction upstream of the grounding line is higher than at other locations causing the ice stream to flow very slowly (about 3 ma^{-1}). At other ice stream grounding lines, the basal traction is smaller allowing the ice to flow across the

grounding line at faster speeds; speeds are on average 400 ma^{-1} (Joughin et al., 2002). The rate of stretching occurring across the grounding line at KIS is greater than at other ice streams due to the increase in speed as the ice goes afloat.

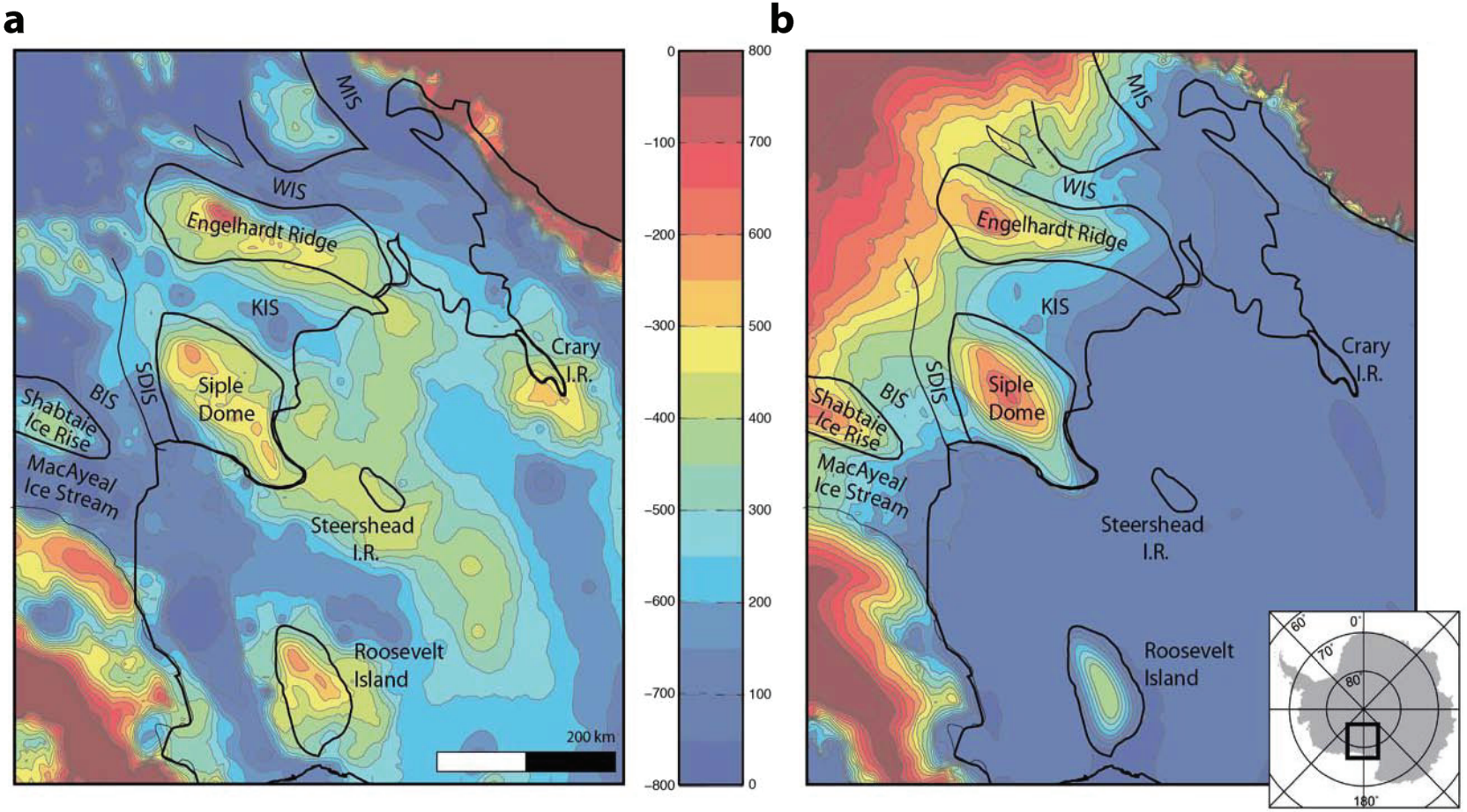

Figure 2: Ross Sea grounding line of the West Antarctic Ice Sheet and outlet ice streams. a) Bed topography b) Surface topography. Data sets from BEDMAP (Le Brocq et al., 2010).).

Fiona Seifert

A set of shore-parallel, long wavelength surface undulations are observed in visible-band imagery of the ice shelf surface downstream of the grounding line at KIS (Figure 3) These features are not observed at the mouths of the other ice streams (Figure 3). The surface undulations have a typical wavelength of ~1.3 km, amplitudes of about 0.5 to 3.0 m, and they repeat only a handful of times before disappearing. Basal crevasses are observed in association with some surface swales but the relationship between the two is not regular. Undulations of this type are seen nowhere else along the coast.

The goal of the present work is to investigate ice mechanics associated with the creation of the surface undulations observed at the KIS grounding line. Classical models of deformation occurring at the grounding line use elastic processes to describe the transition from grounded to floating ice (Holdsworth, 1969; Vaughan, 1995; Sayag and Worster, 2011). In recent years there has been some debate about the necessity of using viscoelastic processes instead to describe this type of deformation (Reeh et al., 2003; Schoof, 2007). Several methods have been developed modeling the ice at the grounding line transition as extensional gravity currents that produce similar surface profiles to the classical elastic models but may capture the material properties of the ice more effectively (Robison et al., 2010; Durand et al., 2009; Schoof, 2011). Since the surface undulations are unusual features, the KIS grounding line provides a unique setting to explore the deformation properties of the ice and determine if the deformation occurring at this

location is related to the elastic or viscous properties of the ice. The study site will be investigated using a combination of remote sensing, field based observations, and mathematical models. Theoretical tools used to develop and test hypotheses for the formation and persistence of these features include models of necking in viscous layers and bending in elastic plates.

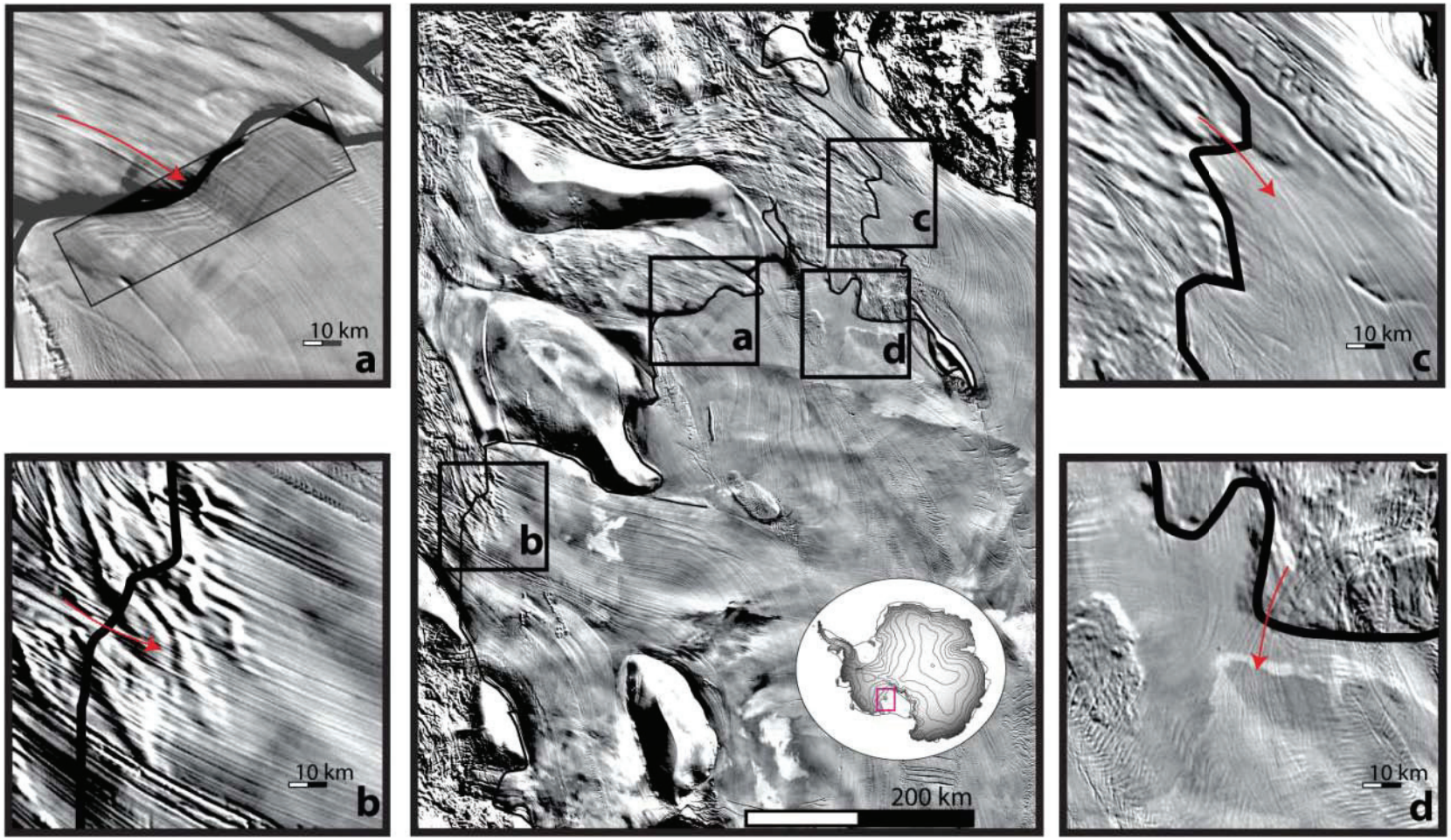

Figure 3: MODIS Mosaic of Antarctica (Scambos et al., 2007) of the Ross Ice Shelf and region (as in Figure 1) highlighting grounding lines. a) Kamb Ice Stream, b) MacAyeal Ice Stream, c & d) Whillans Ice Stream. Surface undulations found at the grounding line of Kamb Ice stream are not found at other ice stream groundings lines in the region. Flow directions are indicated using red arrows.

2 Observations

The surface features investigated here were first observed in Moderate Resolution Imaging Spectro-radiometer (MODIS) images (Scambos et al., 2007) (Figure 3). Though these images provide a general idea of the geometry of the features, their coarse resolution (250 m) precludes detailed mapping of the features. Higher resolution data sets in the form of both satellite and field based observations, have been collected across the features in order to determine the geometry of the grounding line transition, the thickness of the ice, the structure of the ice below the surface, the velocity of the ice, and strain rates. Examination of these data sets, as well as data collected across the neighboring WIS grounding line, provide a detailed description of the features and allow the process associated with their formation to be examined.

2.1 Data sources

The data sources and uses are summarized here. MODIS visible band imagery and the Mosaic of Antarctica (MOA) derived from single MODIS images are used to identify the locations of the undulations and the grounding line positions (Scambos et al., 2007). The resolution of MODIS imagery is 250 m and the error associated with digitizing the grounding line on MODIS imagery is 1 pixel. Higher resolution surface profiles are created using data collected from the Geoscience Laser Altimeter System (GLAS) on NASA's Ice, Cloud, and Land Elevation Satellite (ICESat). Surface elevation is measured over 50-70 m diameter footprints every ~172 m with

an elevation precision of ~ 2 cm and an accuracy of ~ 14 cm (Brunt et al., 2010). Data used here is from release 28 with tide corrections included. Where individual tracks were unavailable, surface profiles were created using digital elevation model produced from a combination of ICESat laser elevation profiles and surface slopes derived from the MOA. Surface profiles have also been measured via GPS on-board sleds driven across the features in November of 2006 (Catania, 2011). The resulting profiles are the highest resolution available with a data point collected ~ 5 m at a 15 m accuracy (Garmin, 2008). Continuous GPS was collected, with the Trimble 5900/R7 equipment, at stations within the strain array over a period of six days during November of 2006. Ice thickness information comes from the BEDMAP data set (Le Brocq et al., 2010).

Arrays of survey marks ("strain grids") were installed by Ginny Catania, Ken Cruikshank, and Christina Hulbe across the KIS and WIS grounding line transitions in November and December of 2006. The KIS array covered an area of 7 km across stream and 11 km in the downstream direction with 1 km spacing (Figure 4). The WIS array was arranged similarly with an area 4 km by 12 km with 1 km spacing; also oriented lengthwise along flow (Figure 4). Repeat 'rapid static' differential GPS surveys were completed in late 2006 and repeated one year later using Trimble 5700/R7 equipment.

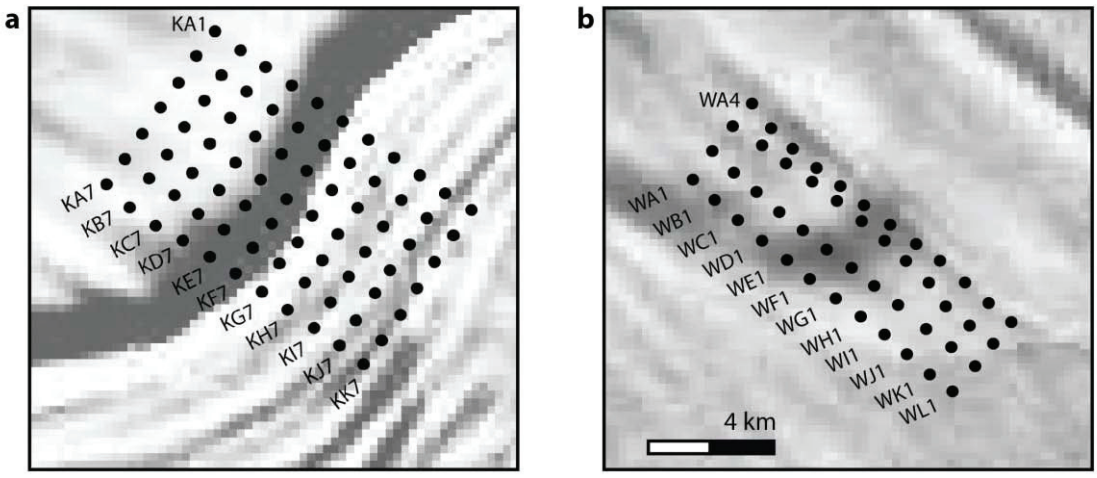

Figure 4: Pole locations for KIS (a) and WIS (b) GPS grids during November and December of 2006.

Base stations for the KIS grid were established each season at KA4, KF4, and KK4. The positions of the base stations were determined by the Natural Resources Canada online Precise Point Positioning (PPP) service. Continuous GPS was collected at the base stations and rover GPS units moved to the other locations within the grid observing the relative locations of the other poles. At each grid point the rover would stop for 15 to 20 minutes. The network resulting from the vectors between grid points and base stations are used to determine the relative positions of all points. The absolute positions are then determined using a network adjustment completed by Dr. Ken Cruikshank using the "TGO", 1.6 Trimble Geomatics Office, software (Cruikshank, 2012) Positioning errors for the base stations KA4 and KF4 in 2006 and 2007 are 0.003 seconds N-S, 0.004 seconds E-W, and 0.014 m in the vertical. Positioning error for base station KK4 in 2006 and 2007 is 0.005 seconds N-S, 0.007 seconds E-W, and .022 m in the vertical.

Base stations were established for the WIS grid at WA2, WF2, and WL2 in November 2006 and November 2007. Collection methods were the same as described above for the KIS grid. Positioning errors for 2006 range from 0.003 to 0.004 m in the N-S and E-W directions at all base stations. The vertical error is .012 m to .017 m. In 2007, the vertical error ranges from .022 m to .036 m and .005 m to .008 m in the N-S and E-W. Some poles in the WIS grid sustained damage between 2006 and 2007. In 2007, severe damage (bending or breakage) to poles WH1 and WH2 made the stations unusable. Moderate damage to poles WA1, WB1, WD1, WE1, WF3, and WE4 affects positioning errors at those stations. Points WC4, WD4, WE3, and WF1 were identified as having poor horizontal quality and therefore unusable (Cruikshank, 2012).

Ground-based ice penetrating radar was used by Ginny Catania to image internal features across the grounding line and undulations during November and December of 2006. Two resistively loaded 2 MHz dipole antennas were attached to sleds and spaced 100 m apart. Samples were taken in the form of 2 kV pulses. The sleds were driven over the area along paths both perpendicular and parallel to the grounding line, collecting radar data and continuous GPS along surface profile. The method of collection was similar to that described by Catania et al. (2008). Data was filtered and processed by Catania and colleagues in the manner described by MacGregor et al. (2011).

2.2 Surface morphology

The features studied here are shore-parallel, long wavelength surface undulations. Similar features are not observed at neighboring grounding lines (Figure 3). The surface features occur within 15 km of the grounding line, repeat only a handful of times (<10), and are not uniformly distributed across the mouth of KIS (Figure 5). The KIS grounding line transition is distinct and has a slope of about 40 m over an ~10 km range (Figure 6). Ice thicknesses, *h*, range from ~550 m in the south to ~650 m in the north (Le Brocq et al., 2010).

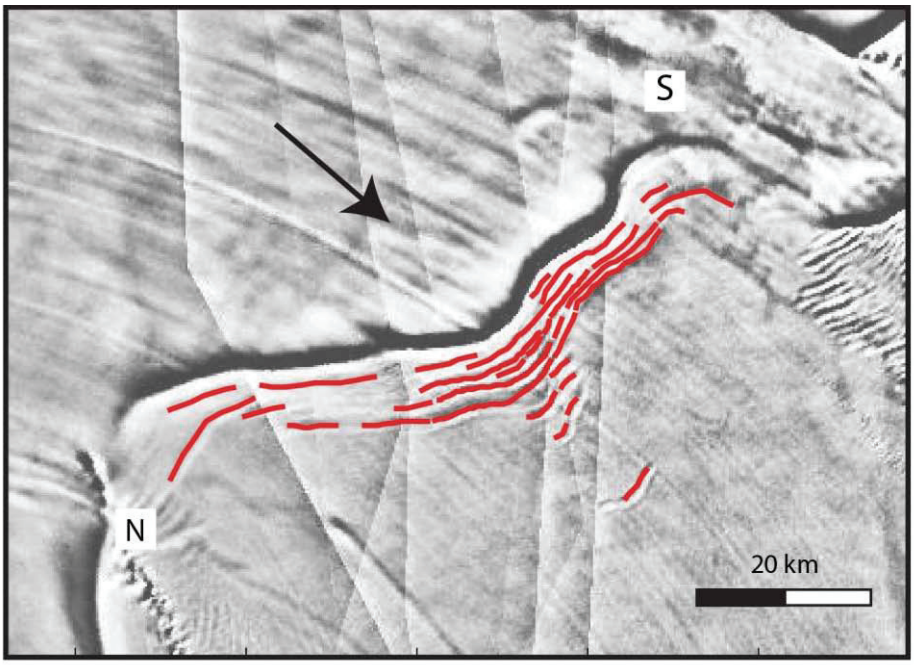

Figure 5: Digitized surface undulations observed at the KIS grounding line overlain on stacked MODIS image (Scambos et al., 2007). The arrow marks the direction of ice flow. N and S refer to north and south directions.

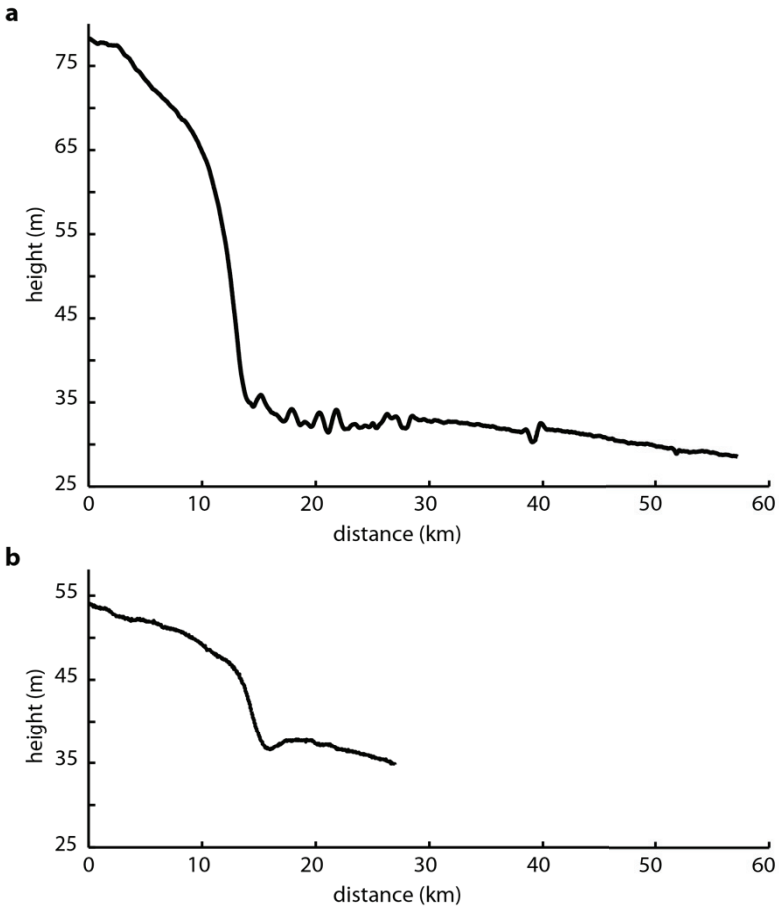

Figure 6: Full length K2 kinematic GPS line (a) and Whillans kinematic GPS line (b) created using the high resolution GPS. Profiles start upstream of the grounding lines and continue on to the Ross Ice Shelf along paths perpendicular to the grounding line. K2 line extends across surface undulations. Data for the WIS profile ends before it reaches 30 km.

Comparison of surface elevation profiles across the grounding line, parallel to the direction of ice flow and perpendicular to the local strikes of the undulations shows that the undulations do not have a uniform geometry (Figure 6). Undulations along the south of the grounding line (orange and red profiles in Figure 7), have relatively large amplitudes, A, of about 0.5 to 3.0 m and wavelengths, λ, of ~1.3 km. Undulations located to the north along the grounding line (the green and blue

profiles in Figure 7) have smaller amplitudes, 0 to 1 m. There may be fewer undulations on the right side of the mouth of KIS or the undulations may simply be smaller and more difficult to identify.

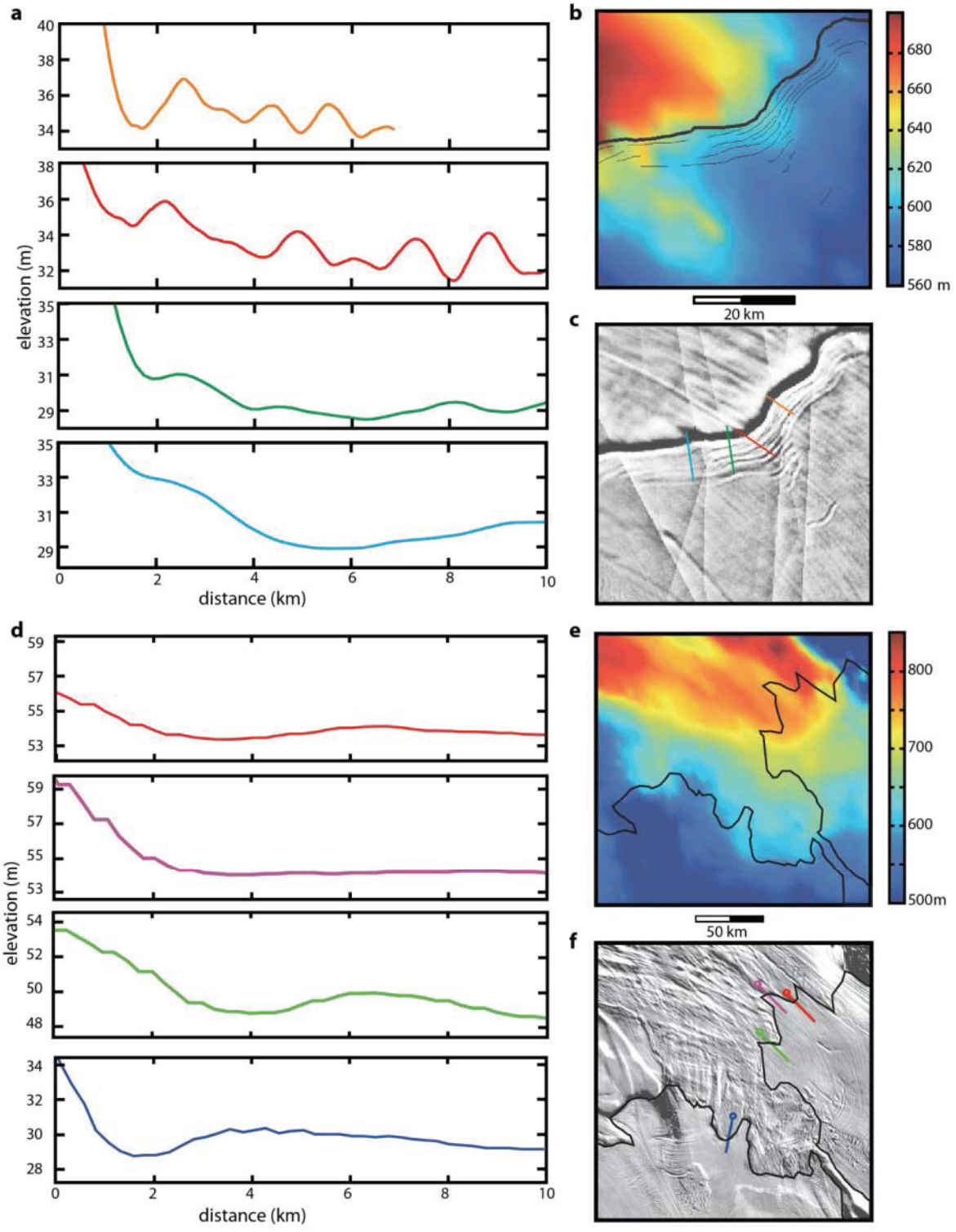
a
b
c
d
e
f
elevation (m)
distance (km)
20 km
50 km
560 m
500m

Figure 7: (previous page) a) – Surface elevation profiles along the KIS grounding line. Starting from the top KA1-KK1 kinematic GPS track, K2 kinematic GPS track, I3e 3030 (2006) ICESat track, and I3j 3149 (2008) ICESat track. b) Ice thickness of KIS from BEDMAP (Le Brocq et al., 2010) c) Locations of surface elevation profiles plotted on a MODIS composite (Scambos et al., 2007). d) Surface elevation profiles along the WIS grounding line (400x vertical exaggeration). Profiles created using DEM data set. e) Ice thickness of WIS from BEDMAP dataset (Le Brocq et al., 2010). f) Locations of surface elevation profiles plotted on the MOA (Scambos et al., 2007).

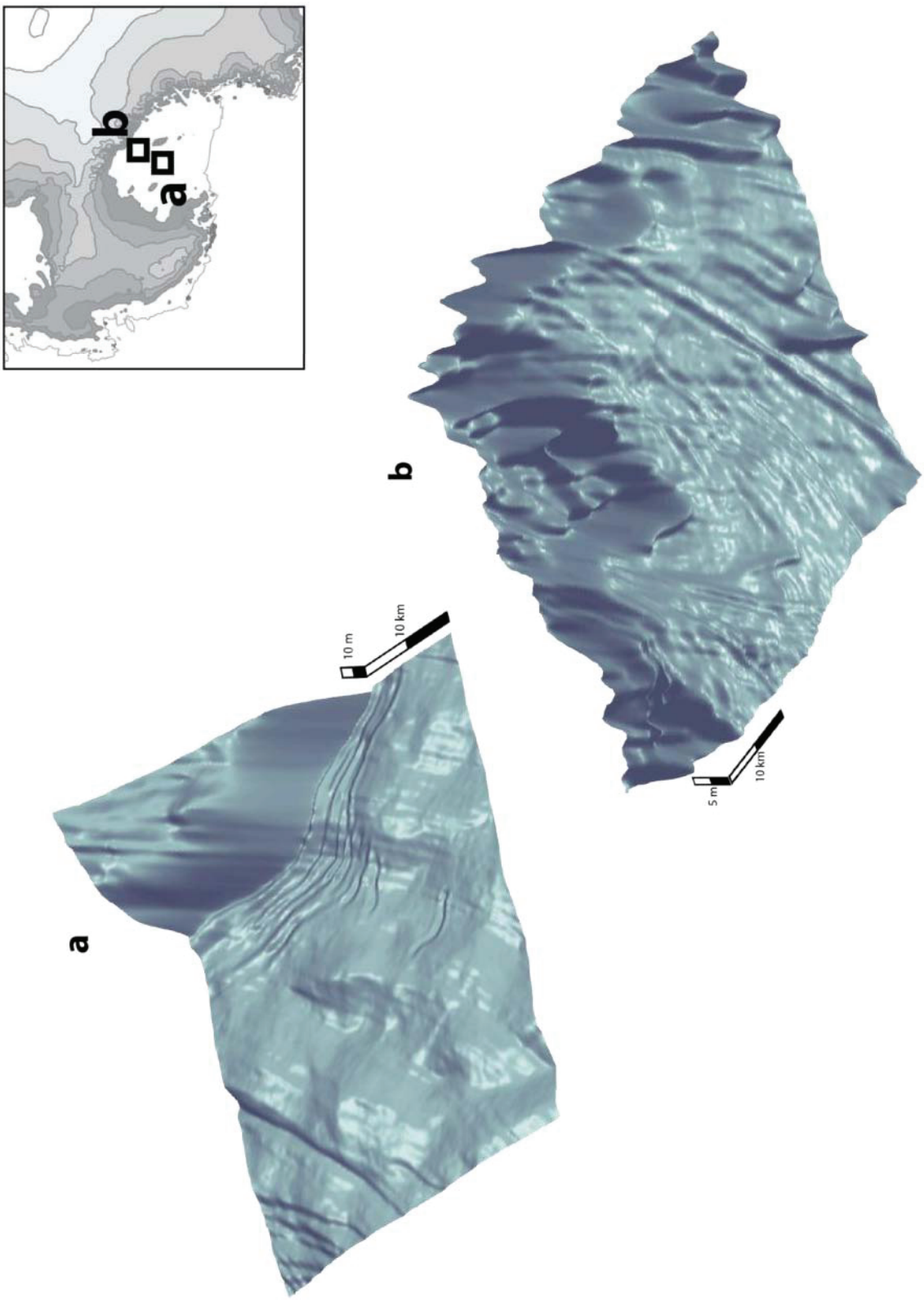
b
a
b
10 km
5 m
10 km
a
10 m
10 km

Figure 8:(previous page) 3D perspective renderings of Kamb (a) and Whillans (b) grounding lines using ICESat elevation data. Panel a corresponds to panel a in Figure 3 and panel b corresponds to panel c in Figure 3. Horizontal scales are the same for both (a) and (b) but the vertical scales are different.

The grounding line transition at WIS is less distinct than at KIS and no repeated surface undulations are evident downstream of the grounding line (Figure 8). Instead, there is a gradual transition from fully grounded to fully floating ice (the transition region is often called an "ice plain"). The slope is about ~13 m over ~10 km (Figure 6). Surface profiles perpendicular to the grounding line derived from the DEM dataset show the single undulation (a dip) that is often observed at the grounded to floating transition (Schoof, 2007; Vaughan, 1995) (Figure 7) . Ice thickness along the WIS grounding line ranges from 500m to 800m (Le Brocq et al., 2010).

2.3 Ice Penetrating Radar

The longest KIS radar profile, called 'K2' here, was collected along flow near the centerline of the ice stream (Figure 9). Regions with abundant basal crevasses correspond to some of the areas with lower surface elevation but there is not a one to one correspondence between the two. The radar profile across a WIS grounding line transition reveals very few basal crevasses, and the crevasses that are observed are not associated with surface lowering (Figure 10).

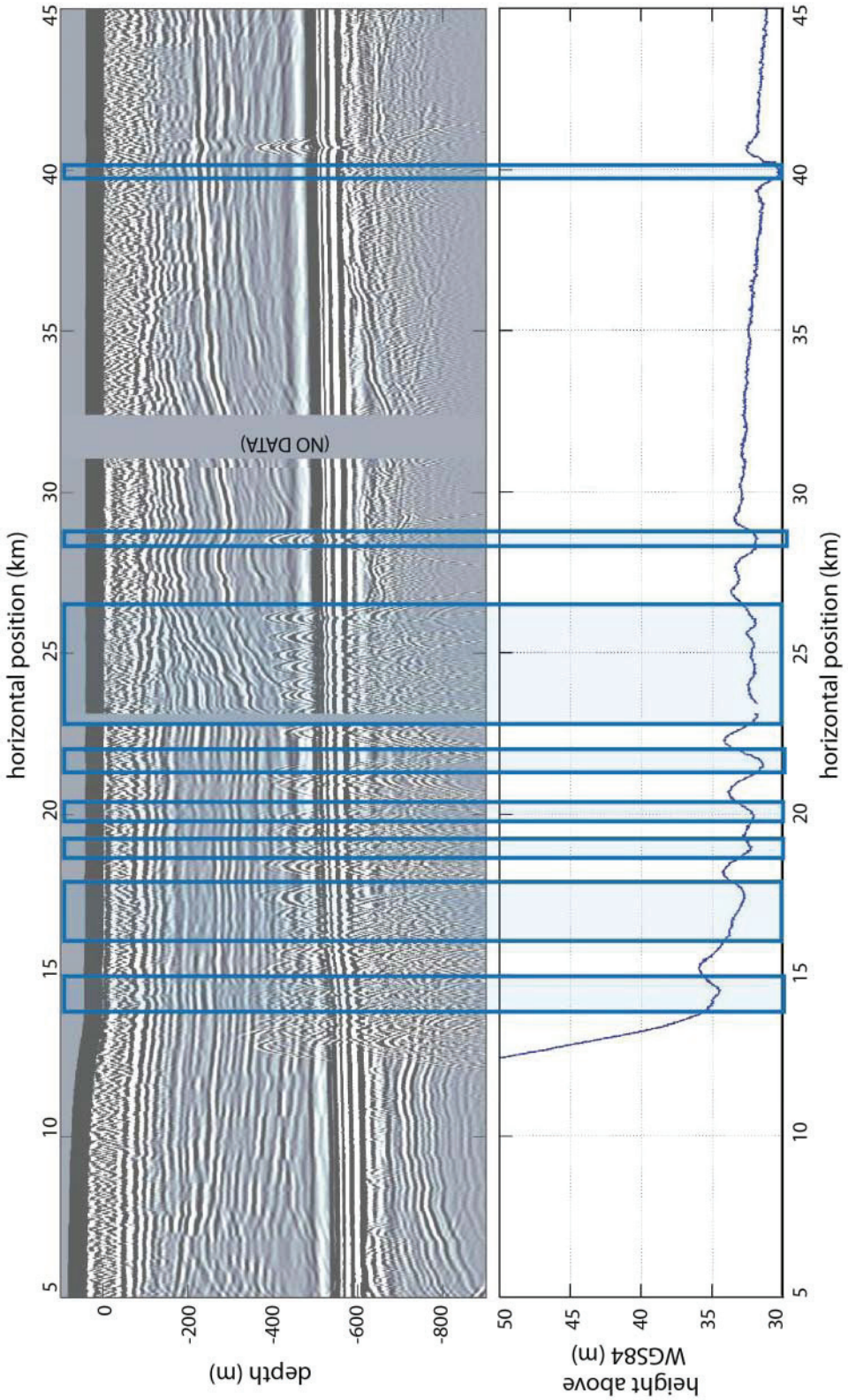
horizontal position (km)
depth (m)
0
-200
-400
-600
-800
(NO DATA)
5
10
15
20
25
30
35
40
45
height above WGS84 (m)
50
45
40
35
30
horizontal position (km)

Figure 9: (previous page) Ice penetrating radar data collected across the KIS grounding line during November of 2006. Radar data was processed by Dr. Ginny Catania at the University of Texas. The lower panel of the graph shows the surface profile created from kinematic GPS collected at the same time as the radar. Blue boxes mark areas of surface lowering. Hyperbolae at depth are associated with basal crevasses. Though areas with heavy crevassing do tend to have a lower profile than those without, there is not a simple correlation between the surface undulations and basal crevasses. For example, the surface profile from km 22 to 26 is similar to the profile from km 29 and 34 but they do not have equivalent basal crevassing. There are areas, such as km 27, where a dip in the surface profile has no associated basal crevassing .

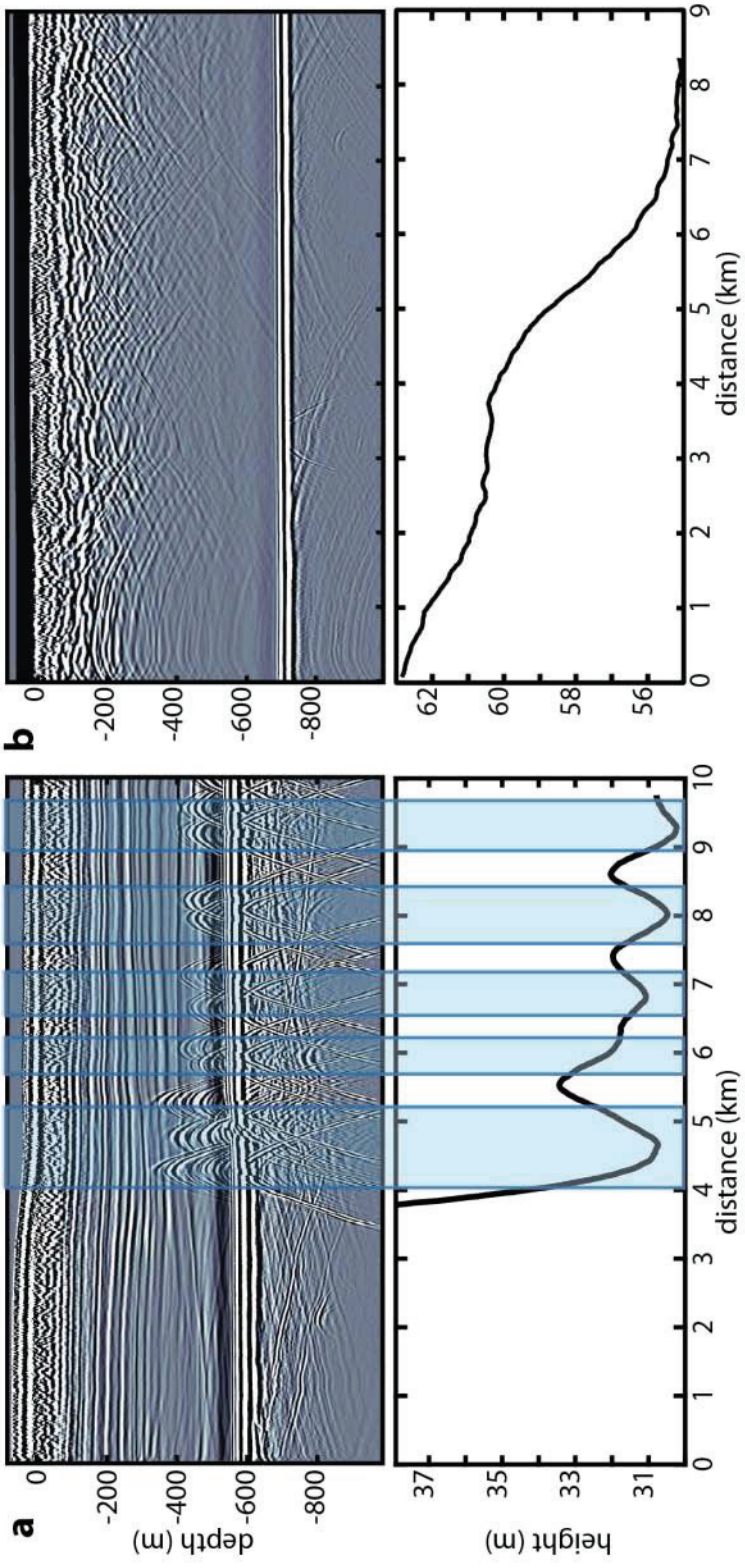

Figure 10: Ice penetrating radar profiles for a) Kamb KA1-KK1, and b) Whillans WA3-WJ3 grid lines (Figure 4) with corresponding surface elevation profiles from kinematic GPS. Crevasses are highlighted. The grounding line for KIS is located at about km 4 on the profile. WIS shows evidence of a grounding zone located from about km 1 to km 6 on the profile.

2.4 Repeat Observations

The position of the undulations with respect to the grounding line and possible change over short time scales can be examined in a few ways. First, an examination of repeat MODIS imagery shows no significant change in shadow location over a period of 24 hours (Figure 11). Thus the features are fixed in space vertically and horizontally on short time scales at the 250 m resolution of the imagery. This is important because it establishes that the undulations are not transient features, ruling out some formation processes.

Repeat-track analysis of ICESat track 3164, using 2b from 2004 and 3j from 2008, shows no significant change in the position of the undulations. The horizontal distance between tracks ranges from 80 – 140 m with a mean value of 100 m separation (Figure 12). This separation causes the tracks to intersect the topography at 20° angle. The initial position of track 3164 2b is offset at 20° from the initial position of track 3164 3J. The tracks then intersect the topography at approximately the same distance along track (Figure 12). The slight variation in track position combined with satellite error could account for the small offset between 2004 and 2008. The slightly larger offset, 2 m, at the grounding line could be due to basal melting there or an error in the tide correction. The undulations appear fixed in the local reference frame on this time scale. This demonstrates that the undulations are neither standing waves excited by tidal motion or transient features.

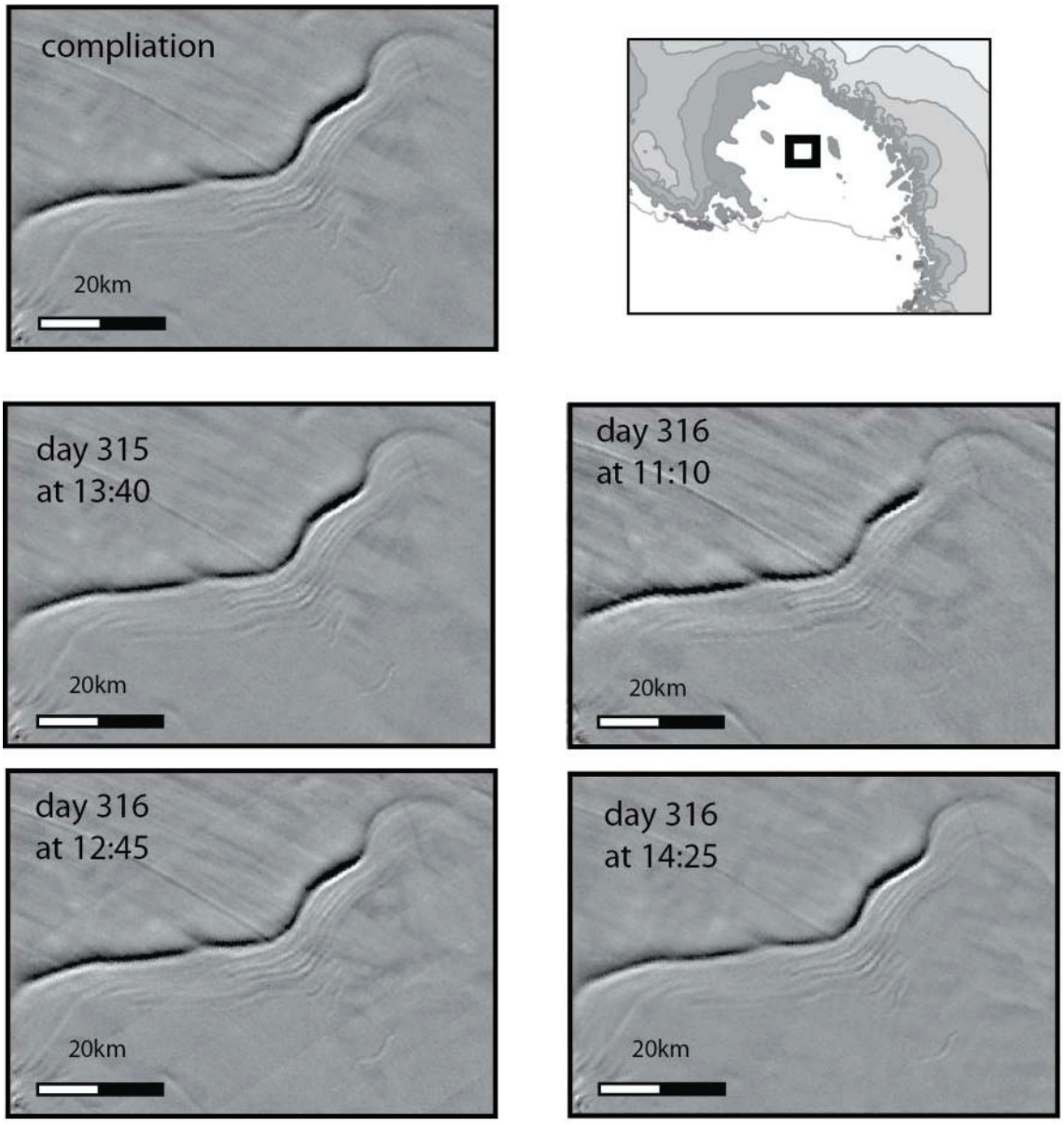

Figure 11: MODIS images from 2001. All four images are stacked in the "compilation." There is no significant change in shadow location among images (Scambos et al., 2007).

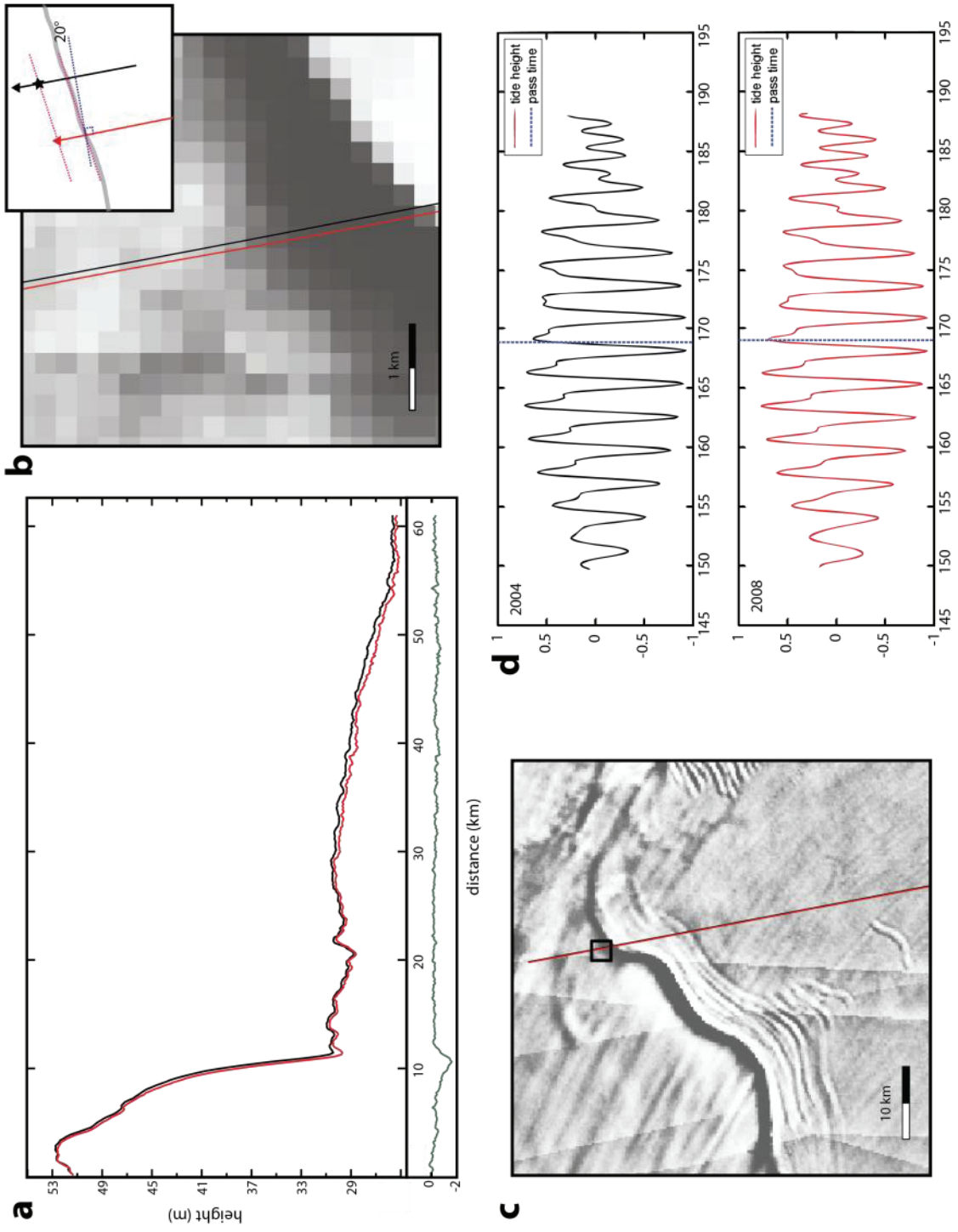
a
height (m)
distance (km)
b
20°
1 km
c
10 km
d
2004
2008
tide height
pass time

Figure 12: Cross track analysis of ICESat track 3164 where red lines are track 3164 3J from 2008 and black lines are track 3164 2b from 2004. a) Along track comparison with green line representing the difference between 3j and 2b (1250x vertical exaggeration). b) Zoom in of location of ICESat tracks with diagram showing the angle the tracks intersect the grounding line. Triangles mark the original starting point to data line. Black star marks the adjusted starting point for track 2b to account for the offset between tracks. c) Location of the tracks relative to the KIS grounding line overlain on stack MODIS image (Scambos et a., 2007). d) Tide predictions for the KIS grounding line intersection with track 3164 in both 2004 and 2008 (Padman, 2012)

Continuous GPS was collected at eight stations within the KIS grid array over the course of six days (Figure 13). Fluctuations to the surface elevation at the six stations match the tide predictions for that time period (Padman, 2012). None of the stations are out of phase suggesting that all stations are rising or falling with the tide in the same manner. If the undulations were standing or traveling waves the stations would move relative to the tide displacement, not all together with it. The features do not appear to be related to changes in the tide height.

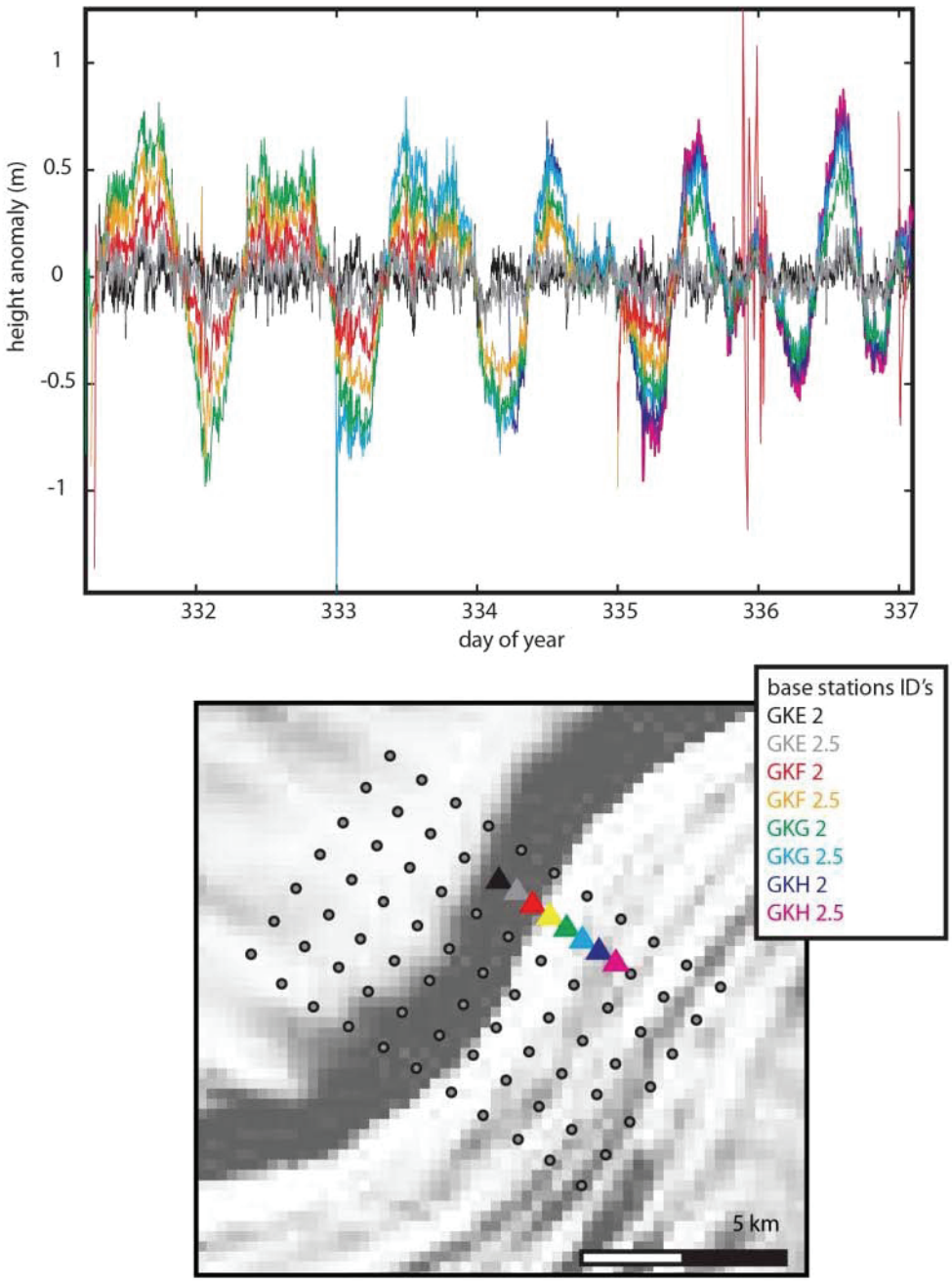

Figure 13: Continuous GPS measurements collected in November and December of 2006 at eight stations within the pole array on KIS. Pole locations are overlain on stacked MODIS image (Scambos et al., 2007). Data shows surface height changes that are congruent with the expected fluctuations in tide height (Padman, 2012).

2.5 Surface velocity

Velocities for positions along the KIS strain grid range from 0.04 $\pm$ 0.03 ma^{-1} to 7.37 $\pm$ 0.11 ma^{-1} (Figure 14). The slowest velocities are found upstream of the grounding line while velocities are largest at the most downstream locations. The largest velocity gradients thus mark the boundary between grounded ice that is frozen to the bed and ice that is floating in the shelf.

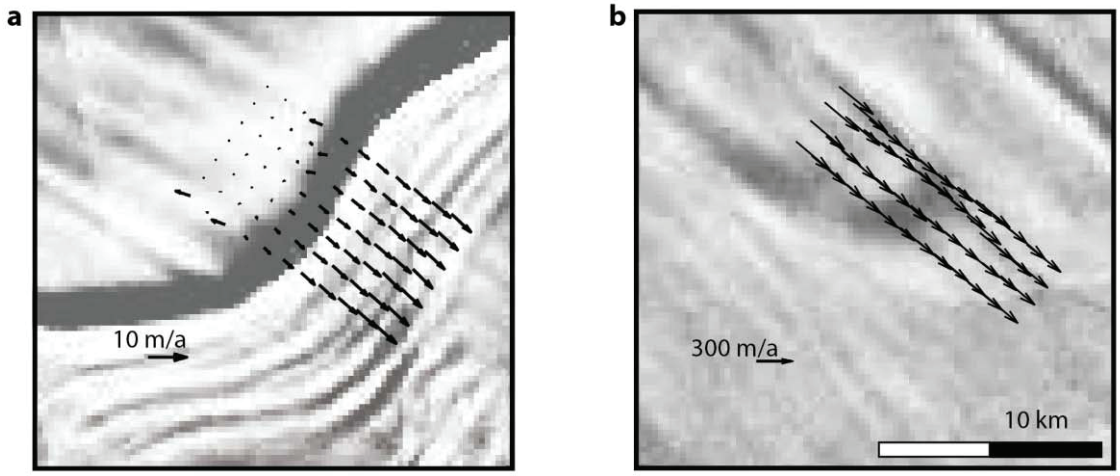

Figure 14: Velocities calculated from rapid static GPS data collected during November of 2006 and 2007 for KIS (a) and WIS (b). Plots overlain on top of stacked MODIS images (Scambos et al, 2007).

Velocities measured in the WIS strain grid between 2006 and 2007 range from 369.22 $\pm$ .06 ma^{-1} to 371.18 $\pm$ .05 ma^{-1}. The velocities of the poles farthest upstream are the lowest and velocities of poles on floating ice are the highest but the difference is small. This pattern is consistent with the transition of low basal traction under the ice stream to even smaller basal traction under the floating ice.

2.6 Strain rates

Assuming the velocity field is continuous, strain rates, $\dot{\epsilon}_{jk}$, at the centroids between four adjacent poles are calculated from the spatial gradients (Cuffey and Paterson, 2010) (Figure 15)

$$\dot{\epsilon}_{jk} = \frac{1}{2}\left[\frac{\partial u_j}{\partial x_k} + \frac{\partial u_k}{\partial x_j}\right] \quad \textbf{(1)}$$

Velocity, $\vec{u}$, has components $[u, v, w]$ in the $[x, y, z]$ directions in a Cartesian coordinate system where the *x*-axis and *y*- axis are in the horizontal plane and the *z*-axis represents the vertical direction. The indices *j* and *k* represent *x*, *y*, or *z* and x_x $=x$, $x_y = y$, and $x_z = z$ (Cuffey and Paterson, 2010). In the *xy* plane, the strain rates are calculated

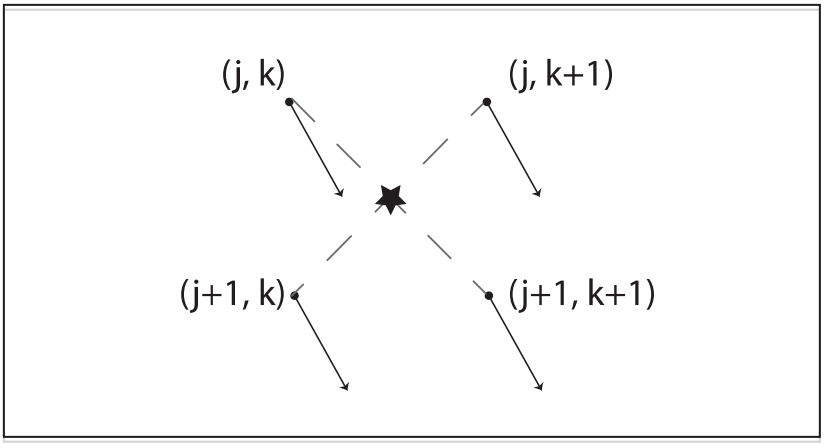

Figure 15: Diagram of centroid position within strain grid.

$$\dot{\epsilon}_{xx} = \frac{1}{2}\left[\left(\frac{u_{(j,k+1)} - u_{(j,k)}}{x_{(j,k+1)} - x_{(j,k)}}\right) + \left(\frac{u_{(j+1,k+1)} - u_{(j+1,k)}}{x_{(j+1,k+1)} - x_{(j+1,k)}}\right)\right] \quad (2)$$

$$\dot{\epsilon}_{yx} = \frac{1}{2}\left[\left(\frac{v_{(j,k+1)} - v_{(j,k)}}{x_{(j,k+1)} - x_{(j,k)}}\right) + \left(\frac{v_{(j+1,k+1)} - v_{(j+1,k)}}{x_{(j+1,k+1)} - x_{(j+1,k)}}\right)\right] \quad (3)$$

$$\dot{\epsilon}_{xy} = \frac{1}{2}\left[\left(\frac{u_{(j+1,k)} - u_{(j,k)}}{y_{(j+1,k)} - y_{(j,k)}}\right) + \left(\frac{u_{(j+1,k+1)} - u_{(j,k+1)}}{y_{(j+1,k+1)} - y_{(j,k+1)}}\right)\right] \quad (4)$$

$$\dot{\epsilon}_{yy} = \frac{1}{2}\left[\left(\frac{v_{(j+1,k)} - v_{(j,k)}}{y_{(j+1,k)} - y_{(j,k)}}\right) + \left(\frac{v_{(j+1,k+1)} - v_{(j,k+1)}}{y_{(j+1,k+1)} - y_{(j,k+1)}}\right)\right] \quad (5)$$

Solving the strain tensor

$$\dot{\epsilon} = \begin{bmatrix} \dot{\epsilon}_{xx} & \dot{\epsilon}_{xy} \\ \dot{\epsilon}_{yx} & \dot{\epsilon}_{yy} \end{bmatrix} \quad (6)$$

for its eigenvectors and eigenvalues produces principal strain rates in the horizontal plane (Figure 16).

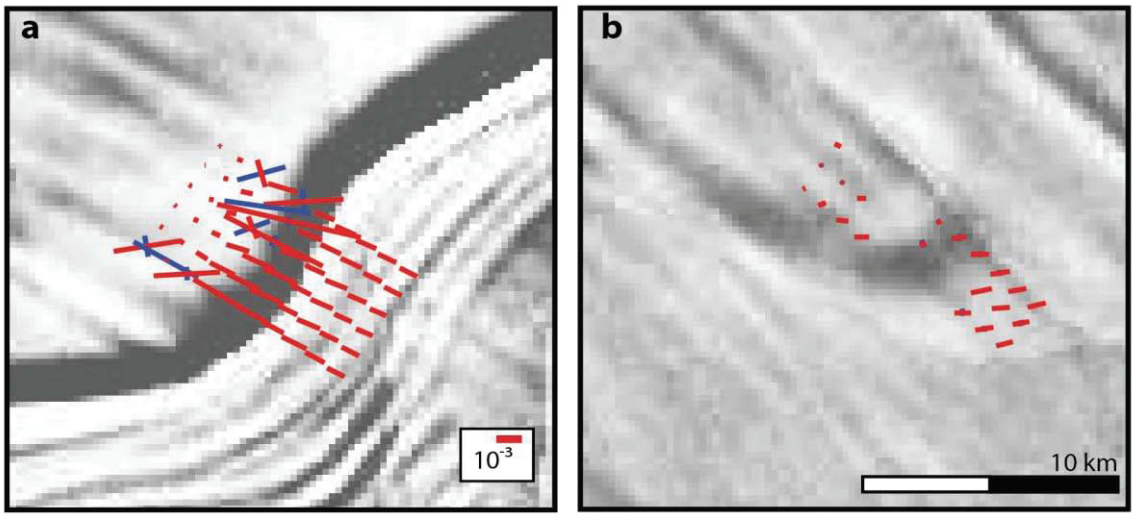

Figure 16: Principal strain rates calculated for quadrilaterals in the strain grids using rapid static GPS measured across the KIS (a) and the WIS (b) grounding line during November of 2006 and 2007. Plots overlain on top of stacked MODIS images (Scambos et al., 2007).

The deformation pattern for both the KIS and WIS grounding lines is extension parallel to the flow direction with the largest strain rates are across the grounding line (Figure 17). The principal extensive strain rates for the KIS grid range from $6.00 \times 10^{-6} \pm 1.12 \times 10^{-3}$ a^{-1} to $5.80 \times 10^{-3} \pm 2.14 \times 10^{-4}$ a^{-1} with a mean of $1.00 \times 10^{-3} \pm 5.65 \times 10^{-4}$ a^{-1} (Appendix F). The principal extensive strain rates for the WIS grid range from $7.83 \times 10^{-5} \pm 6.90 \times 10^{-7}$ a^{-1} to $8.01 \times 10^{-4} \pm 3.70 \times 10^{-7}$ a^{-1} with a mean of $4.87 \times 10^{-4} \pm 6.65 \times 10^{-7}$ a^{-1} (Appendix G).

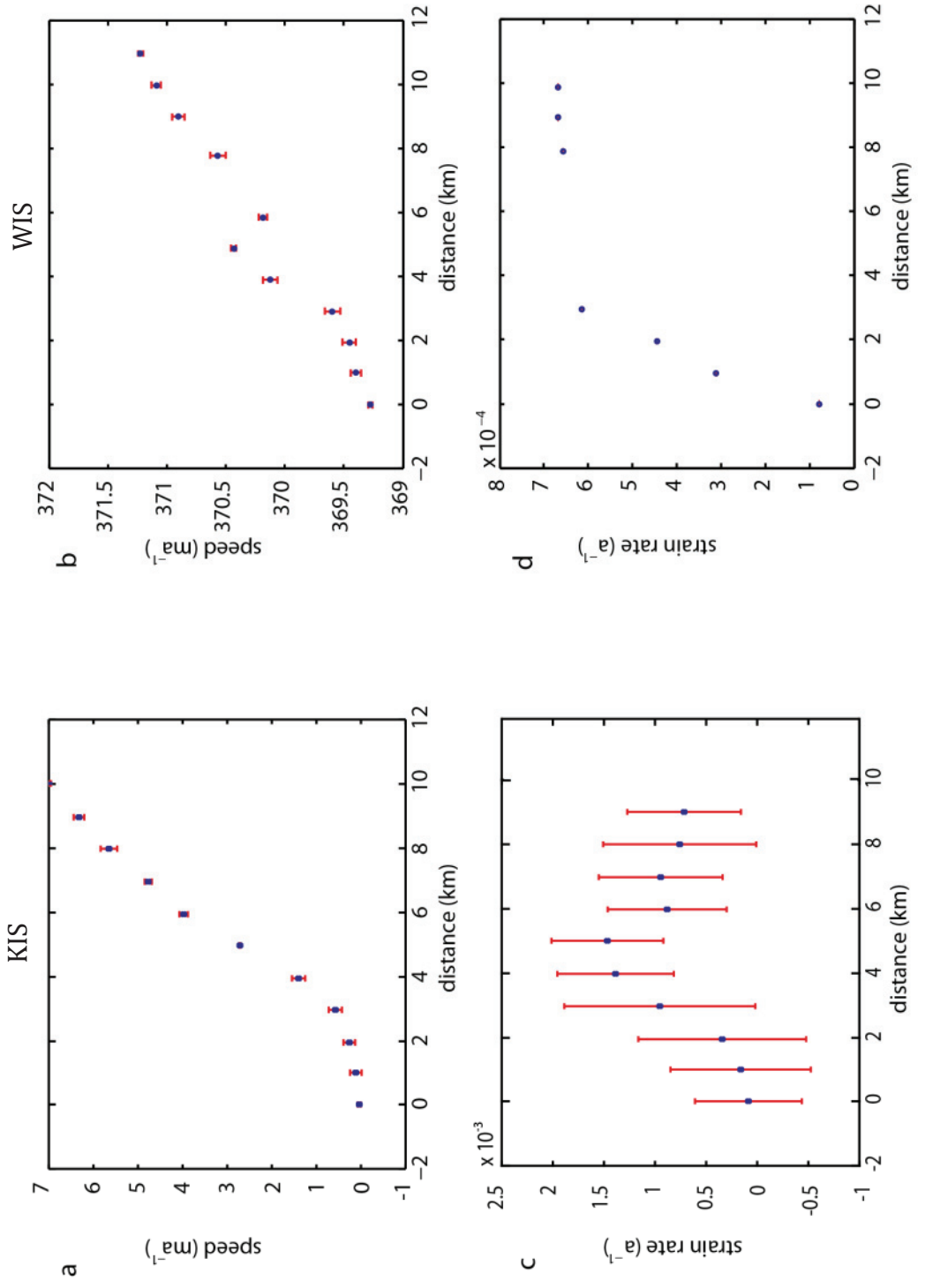
KIS
WIS
a
b
c
d
speed (ma^{-1})
strain rate (a^{-1})
distance (km)
x 10^{-3}
x 10^{-4}

Figure 17: Velocity (a, b) and principal extensive strain rates (c,d) calculated at the centroids across the KIS and WIS grounding lines (Appendix F, Appendix G). Propagated errors are shown as vertical bars. The error for (d) is equivalent to the width of the marker. The data are as in figure (16) and the profiles are for the K*6 grid line of KIS and the W*2 grid line of WIS. The gounding line transition is at approximately km 5 for both the KIS and WIS profiles.

The large number of damaged poles in the WIS grid led to areas that are poorly resolved by the quadrilateral calculation, an alternative calculation is performed using triangulation. A Delaunay triangulation is completed on the grid using the Matlab function Delaunay (Figure 18). In a Delaunay triangulation no triangle vertex is contained within another triangle's circumscribed circle and no side of any triangle is cut by another triangle (Cai et al., 2008). The centroid of each triangle is

$$\mathrm{x}_b = \frac{x_1 + x_2 + x_3}{3} \quad \textbf{(7)}$$

$$\mathrm{y}_b = \frac{y_1 + y_2 + y_3}{3} \quad \textbf{(8)}$$

in which the subscript indicates the vertex number (Figure 18). The velocity of each vertex is

$$u_i = \Delta x_i \dot{\epsilon}_{xx} + \Delta y_i \dot{\epsilon}_{xy} + u_b \quad \textbf{(9)}$$

$$v_i = \Delta x_i \dot{\epsilon}_{yx} + \Delta y_i \dot{\epsilon}_{yy} + v_b \quad \textbf{(10)}$$

in which Δx_i and Δy_i represent the distance from the vertex to the centroid, $\dot{\epsilon}_{ii}$ represents the strain rate components for the centroid, and u_b and v_b represent the

velocity component for the centroid. The system of equations for each centroid is thus

$$\begin{bmatrix} u_b \\ v_b \\ \dot{\epsilon}_{xx} \\ \dot{\epsilon}_{xy} \\ \dot{\epsilon}_{yx} \\ \dot{\epsilon}_{yy} \end{bmatrix} = \begin{bmatrix} \Delta x_1 & \Delta y_1 & 0 & 0 & 1 & 0 \\ 0 & 0 & \Delta x_1 & \Delta y_1 & 0 & 1 \\ \Delta x_2 & \Delta y_2 & 0 & 0 & 1 & 0 \\ 0 & 0 & \Delta x_2 & \Delta y_2 & 0 & 1 \\ \Delta x_3 & \Delta y_3 & 0 & 0 & 1 & 0 \\ 0 & 0 & \Delta x_3 & \Delta y_3 & 0 & 1 \end{bmatrix}^{-1} \begin{bmatrix} u_1 \\ v_1 \\ u_2 \\ v_2 \\ u_3 \\ v_3 \end{bmatrix} \quad \textbf{(11)}$$

which can be solved for the centroid velocity and strain rates (Cai et al., 2008). Principal strain rates are again the eigenvectors of (6).

Velocities and strain rates computed using triangulation are similar to those computed using quadrilaterals, although the spatial coverage is better with the former than the latter (Figure 18). The extension going from grounded to floating ice follows a more expected pattern (with the highest strain rates across the transition) here than in the quadrilateral-derived result. Velocities calculated at the centroids of the Delaunay triangles are less variable than those calculated at the quadrilateral centroids due to an increase in the number of centroids for the Delaunay method (Figure 18).

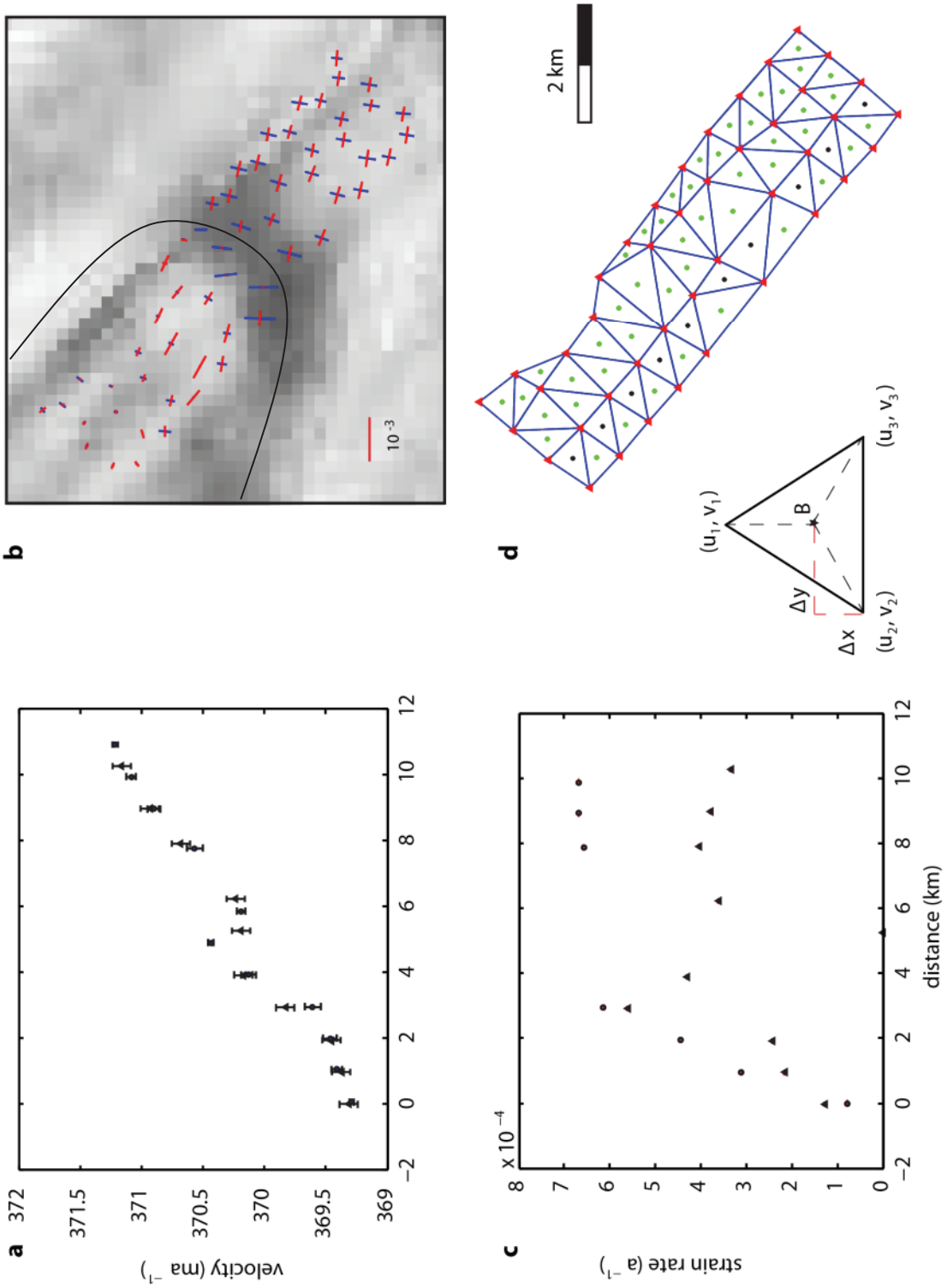
a
b
c
d
velocity (ma⁻¹)
372
371.5
371
370.5
370
369.5
369
−2
0
2
4
6
8
10
12
10⁻³
strain rate (a⁻¹)
x 10⁻⁴
8
7
6
5
4
3
2
1
0
distance (km)
2 km
(u1, v1)
(u2, v2)
(u3, v3)
B
Δy
Δx

Figure 18: Velocity (a) and principal strain rates (b, c) measured across WIS grounding lines (Appendix H). Strain rates calculated using triangulation (b) are overlain on a stacked MODIS image with estimated grounding line position in black (Scambos et al., 2007). The principal extensive strain rates are plotted in (c). Values calculated using the quadrilateral method are marked with dots and values calculated using the triangulation method are marked with triangles. Propagated errors are shown as vertical bars. The error for (c) is equivalent to the width of the marker. The quadrilaterl data are as in figure (17). The gounding line transition is at approximately km 5 . Centroids from the Delaunay triangluation (d) are marked with green stars and black dots. The black centroids are used to create triangulation method profiles and the locations are comparble to the centoids along the W*2 grid line.

3 Analysis

Several models of the grounding line transition and ice shelf are developed to evaluate the relationship between material properties and the observed surface morphology. A comparison of the surface morphology to possible changes in the density of the ice or the position of the grounding line is completed. Elastic models presented here include a thin clamped plate, a point load with a fixed location, and a point load with a free boundary. The viscous model used for this analysis examines the observed surface features as amplified instabilities caused by the transition from grounded to floating ice. All of the models use the data presented previously in chapter two.

3.1 Density Variation

3.1.1 Isostatic and Hydrostatic equilibrium

When a layer is in a state of isostatic equilibrium, any variations in surface height must reflect variations in density, thickness, or a combination of both (Figure 19) (Turcotte and Schubert, 2002). If the surface undulations at the KIS grounding line were compensated by variation in thickness there would be varying bottom relief of 0 to 29 m. The source of such variations in ice thickness might be basal crevasses or a special pattern in basal melting. Crevasses are present under some surface swales but they would need to be very wide, and remain wide well into the underside of the ice shelf (Figure 9). Alternatively, narrow crevasses could locally

modify the bulk density of the column. When a crevasse forms underneath the ice, the denser seawater can infiltrate the ice creating an area with a larger bulk density. The new density is

$$\rho_3 = \rho_2 \left(\frac{d}{A + d} \right) \quad \textbf{(12)}$$

in which ρ_3 represents the density of the thicker/higher column of ice, ρ_2 represents the density of the thinner/shorter column of ice, A represents the amplitude of the undulations, and d represents the thickness of the surrounding ice not including amplitude. With an ice thickness of 600m and surface undulations with maximum amplitude of 3m, the density of the ice only needs to be changed by 0.5% to produce the observed surface lowering.

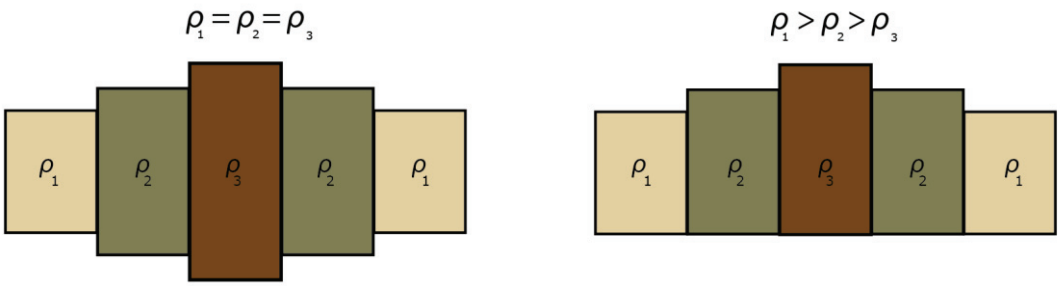

Figure 19: Diagram on left depicts Airy's method of compensation where the density is the same throughout and variations in surface topography are matched by equivalent basal variation. The diagram to the right depicts Pratt's method of compensation where variations in topography are representative of variations in density (Turcotte and Schubert, 2002).

3.1.2 Changes to the grounding line

The surface features may be evidence of cyclic grounding line events due to an unknown process. One possible mechanism causing the surface pattern could be episodic changes in the thinning rate, in which local highs would represent periods with a lower thinning rate and troughs would represent periods with a higher thinning rate. Using a speed of 7.0 ma^{-1}, a strain rate of 1.0 x 10^{-3} a^{-1} , and holding the grounding line position fixed, it would take approximately 190 years to transition from a trough to an adjacent peak in the observed undulations. It is unclear what kind of process would cause cycles in the thinning rate on this timescale and this idea is thus discounted.

The surface variation could also be caused by periodic changes in the grounding line position. The current thinning rate is approximately 0.6 ma^{-1} across the grounding line of KIS, which is higher than the thinning rates upstream or

downstream of the grounding line. If the grounding line stayed in place with a steady thinning rate for about 5 years, and then instantly shifted inland the distance of the wavelength of the observed features, about 1 km, a relatively higher elevation where the ice had been grounded previously and a trough at the former grounding line position would be formed. If this process repeated for approximately 30 years it could create the observed surface variability. There are currently no identified processes that would cause the grounding line position to change in this manner.

3.2 Elastic bending

3.2.1 Euler-Bernoulli beam bending

Euler-Bernoulli beam bending is a special case of linear elastic beam theory which describes the deflection of an elastic beam subject to lateral loading (Turcotte and Schubert, 2002). The theory is limited to cases where displacement is small compared to the length and in which the beam experiences no shear deformation. Taking inertial effects to be small, the relationship between deformation and the applied load q is

$$\frac{d^2}{dx^2}\left(EI\frac{d^2w}{dx^2}\right) = q \qquad \textbf{(13)}$$

for the static beam bending case in which *w(x)* describes the deflection of the beam. The elastic modulus E and the area moment of inertia of the beam I remain constant throughout the beam (Turcotte and Schubert, 2002; Fowler, 2005).

3.2.2 Uniform load

The transition at the grounding line can be represented as a thin plate clamped at one edge (over the grounding line) with a uniform load across the plate (Turcotte and Schubert, 2002). Repeat observations of the surface undulations show that they are fixed in time and space over the timescales were completed. Therefore the use of a static beam bending equation is reasonable. Where the plate is clamped $w = \frac{dw}{dx} = 0$ and $x = 0$ (Figure 20). At the end of the plate, $x = L$, there is no external torque therefore $\frac{d^2w}{dx^2} = 0$. The velocity of the beam is zero making $\frac{dM}{dx} = 0$, and $\frac{d^3w}{dx^3} = 0$. With those boundary conditions and a uniform load, the solution to (13) is

$$w(x) = \frac{x^2}{D}\left(\frac{x^2}{24} - \frac{Lx}{6} + \frac{L^2}{4}\right) \quad \textbf{(14)}$$

with a flexural rigidity of

$$D = \frac{Eh^3}{12(1 - v^2)} \quad \textbf{(15)}$$

in which v represents Poisson's ratio and h represents the thickness of the ice (Turcotte and Schubert, 2002). The load in this case is

$$q = -\frac{\left((\rho_{sw} - \rho_i)g\right)}{L} \quad \textbf{(16)}$$

in which ρ_{sw} represents the density of sea water, ρ_i represents the density if ice, g represents acceleration due to gravity, and L represents the length of the plate (Turcotte and Schubert, 2002).

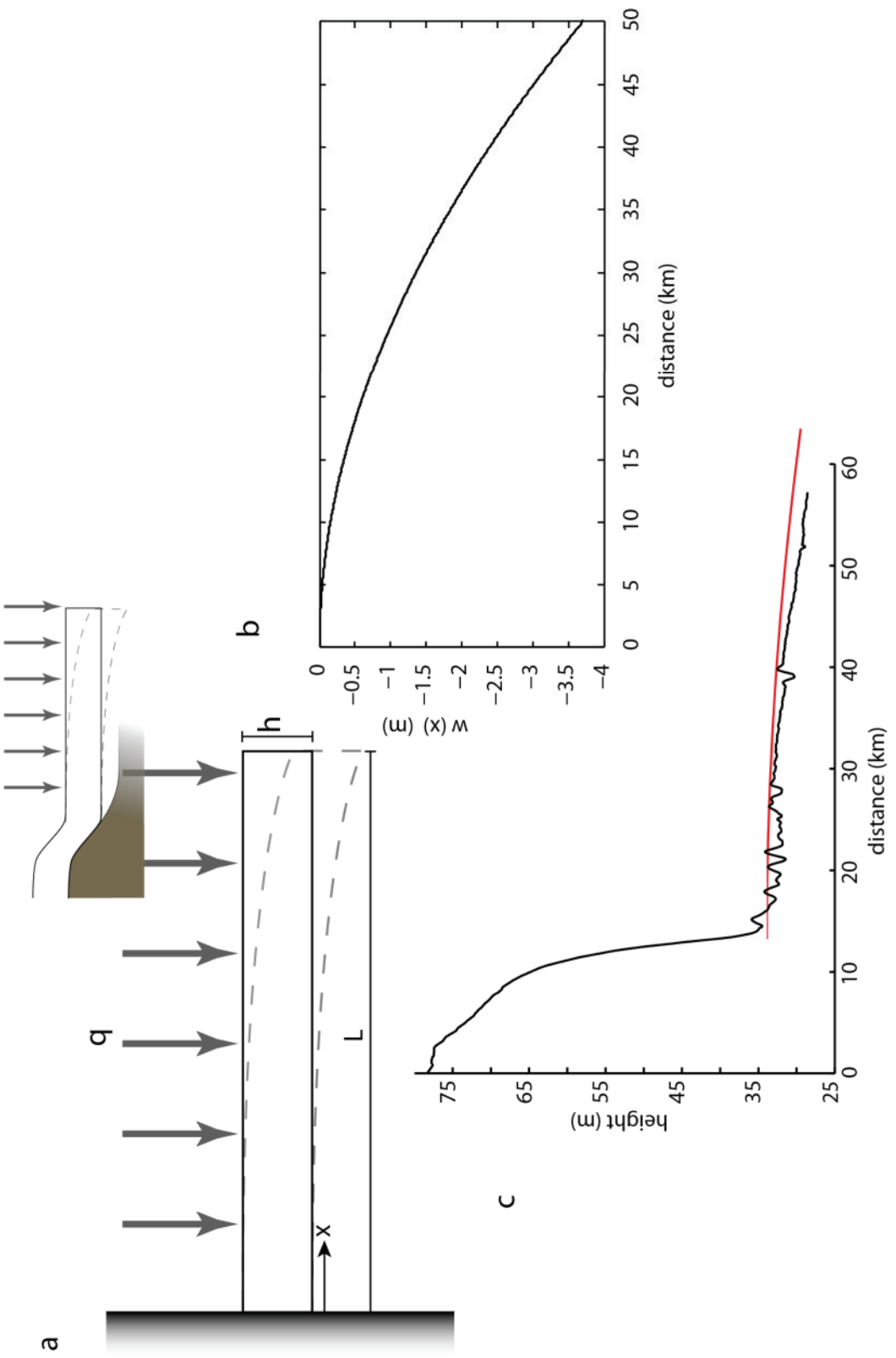
a
q
h
L
x
b
w (x) (m)
distance (km)
c
height (m)
distance (km)

Figure 20: a)- Force diagram modeling a uniformly loaded plate clamped at one end with length L and thickness *h* (Turcotte and Schubert, 2002). b) Predicted profile of the KIS grounding line created from the thin clamped plate model (5500x vertical exaggeration). c) Profile b) overlain on top of the kinematic GPS line K2 with (800x vertical exaggeration).

Conditions at the KIS grounding line are represented using 1025 kg m^{-3} for the density of sea water, a Poisson's ratio of 0.314, an elastic modulus of 9 x 10^9 Pa, a thickness of 600 m, a beam length of 800 km (L), and a depth integrated value of 910 kg m^{-3} for the density of ice. The resulting profile deflects downward, producing a deflection near the grounding line of appropriate magnitude but does not produce undulations as observed at KIS (Figure 20).

3.2.3 Point load with a fixed boundary

Another solution to (13) examines the effect of a single point load on a semi-infinite elastic beam resting on a horizontal elastic foundation (Figure 21). The model is made comparable to an ice shelf over water by inverting the system, shifting the origin to line up with the point load, and eliminating the left half of the symmetry (Holdsworth, 1969; Vaughan, 1995) . The deflection of the beam can then be describe by

$$\frac{d^2w}{dx^2} = -\frac{(1-v^2)}{EI}M(x) \qquad \textbf{(17)}$$

and

$$\frac{d^4w}{dx^4} = -\frac{(1-v^2)}{EI}\rho_{sw}g\big(w_a - w(x)\big) \quad \textbf{(18)}$$

in which *M(x)* is the bending moment at *x* and w_a represents the unbent position of the beam (Figure 21). The solution to the system of equations is (Holdsworth, 1969; Vaughan, 1995)

$$w(x) = w_a\left(1 - e^{-\beta x}(\cos\beta x + \sin\beta x)\right) \quad \textbf{(19)}$$

in which the coefficient β is the damping factor

$$\beta^4 = 3\frac{\rho_{sw}g(1-v^2)}{Eh^3} \quad \textbf{(20)}$$

The KIS grounding line is modeled using w_a ranging from -1 to 1 to represent a change in tide height. The deflection of the model, from -1 to 1, is limited to a region within about 10 km of the grounding line and does not model the surface undulations observed (Figure 21).

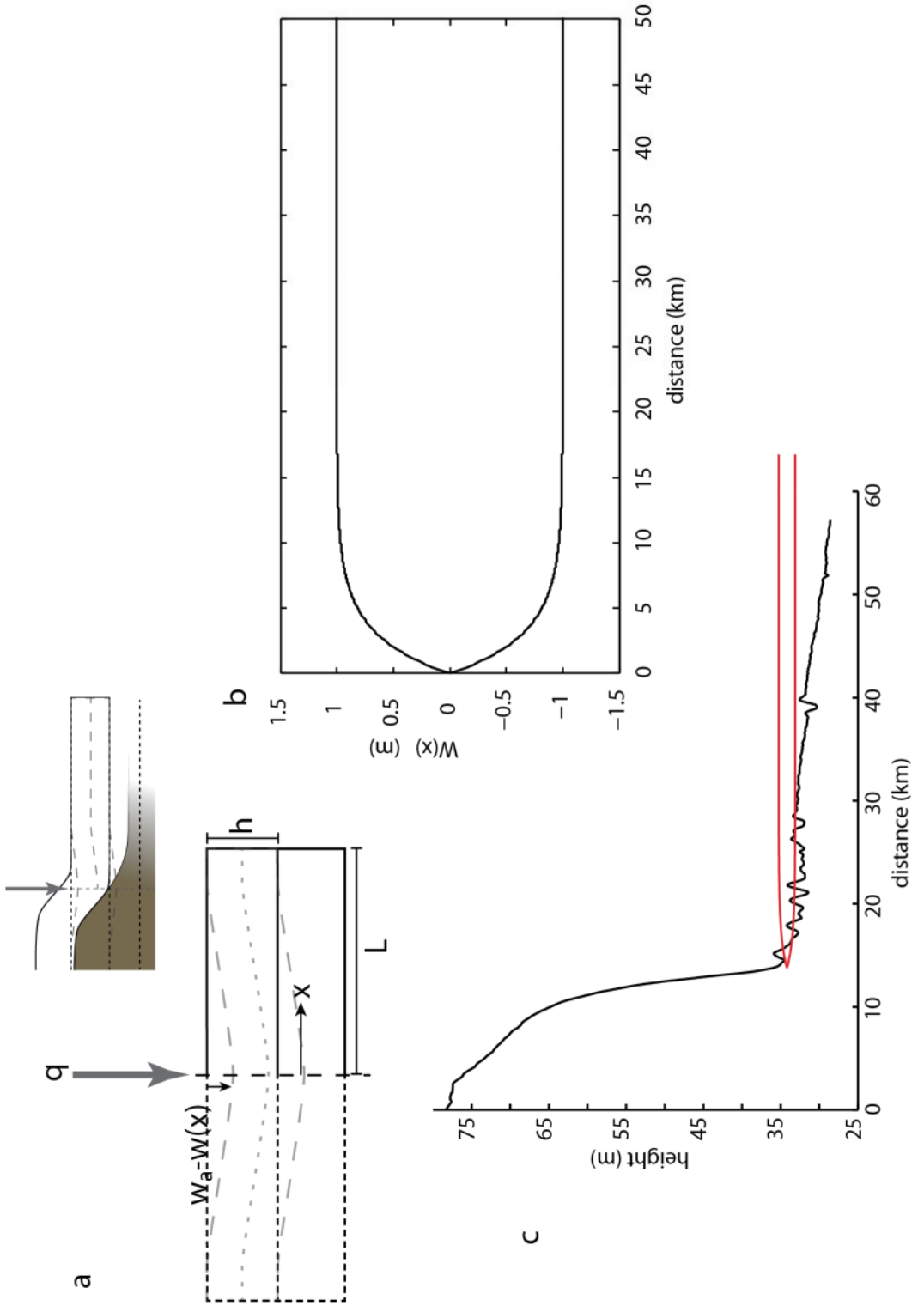
a
q
h
L
x
W_a-W(x)
b
W(x) (m)
1.5
1
0.5
0
−0.5
−1
−1.5
0
5
10
15
20
25
30
35
40
45
50
distance (km)
c
height (m)
75
65
55
45
35
25
0
10
20
30
40
50
60
distance (km)

Figure 21: a)- Force diagram modeling an elastic beam resting on an elastic foundation with a point load at the grounding line, length L, and thickness h (Holdsworth, 1969; Vaughan, 1995). b) Predicted profile of the KIS grounding line created from a) (8000x vertical exaggeration). c) Profile b) overlain on top of the kinematic GPS line K2 (700x vertical exaggeration).

3.2.4 Model of a point load with a free boundary

The transition can also be represented as a beam with a point load resting on a split foundation. In this solution to the beam equation, one half of the beam rests on an elastic solid and one part floats on a denser fluid with a free boundary at the grounding line rather than a fixed boundary. Beginning with (13) and following Sayag and Worster (2011) for a long ice shelf in which the grounding line is below the surface of the ocean, the deflection seaward of the grounding line is

$$y_1 = \frac{1}{2} - \frac{\rho_i}{\rho_{sw}} + e^{-\gamma_1 x}\left[\cos(\gamma_1 x)\left(\frac{\rho_i}{\rho_{sw}}\right) - \frac{\sin(\gamma_1 x)}{1+\frac{\gamma_1}{\gamma_0}}\left(\frac{\gamma_0^2\rho_i}{\gamma_1^2 k_0} + \frac{\gamma_1}{\gamma_0}\left(\frac{\rho_i}{\rho_{sw}}\right)\right)\right] \quad (21)$$

in which only the leading term in the series expansion has been retained. The parameter k_0 represents a stiffness coefficient of the bed beneath the ice stream, the coefficients γ_0 and γ_1 are

$$\gamma_0 = \frac{1}{l\sqrt{2}}\left(\frac{k_0}{\rho_{sw} g}\right)^{\frac{1}{4}} \quad (22)$$

$$\gamma_1 = \frac{1}{l\sqrt{2}} \quad (23)$$

and the bending length scale is

$$l = \left(\frac{D}{\rho_{sw} g}\right)^{\frac{1}{4}} \quad \textbf{(24)}$$

A stiffness coefficient of 9114 $kgm^{-2}s^{-2}$ is used to representative a soft bed underneath the grounded portion of the ice stream (Sayag, 2011).

Thus configured, the model yields a short wavelength undulation with an amplitude of about 2 m immediately downstream of the grounding line. Thereafter the bending (the second term on the right hand side of (21) is damped according to (23). In contrast to this elastic model prediction, the observed undulations do not decay rapidly but instead have similar amplitudes over a reach that extends many ice thicknesses away from the grounding line. While the relatively short wavelength predicted by the split foundation model is similar to the first undulation at the KIS grounding line, it does not fit the longer wavelength dip observed at both the WIS and KIS grounding lines (Figure 7). Were the split foundation model correct, it would predict an observed wavelength at both grounding lines. The Holdsworth (1969) model produces a better result for the elastic deformation at both locations but does not reproduce the series of undulations observed at KIS

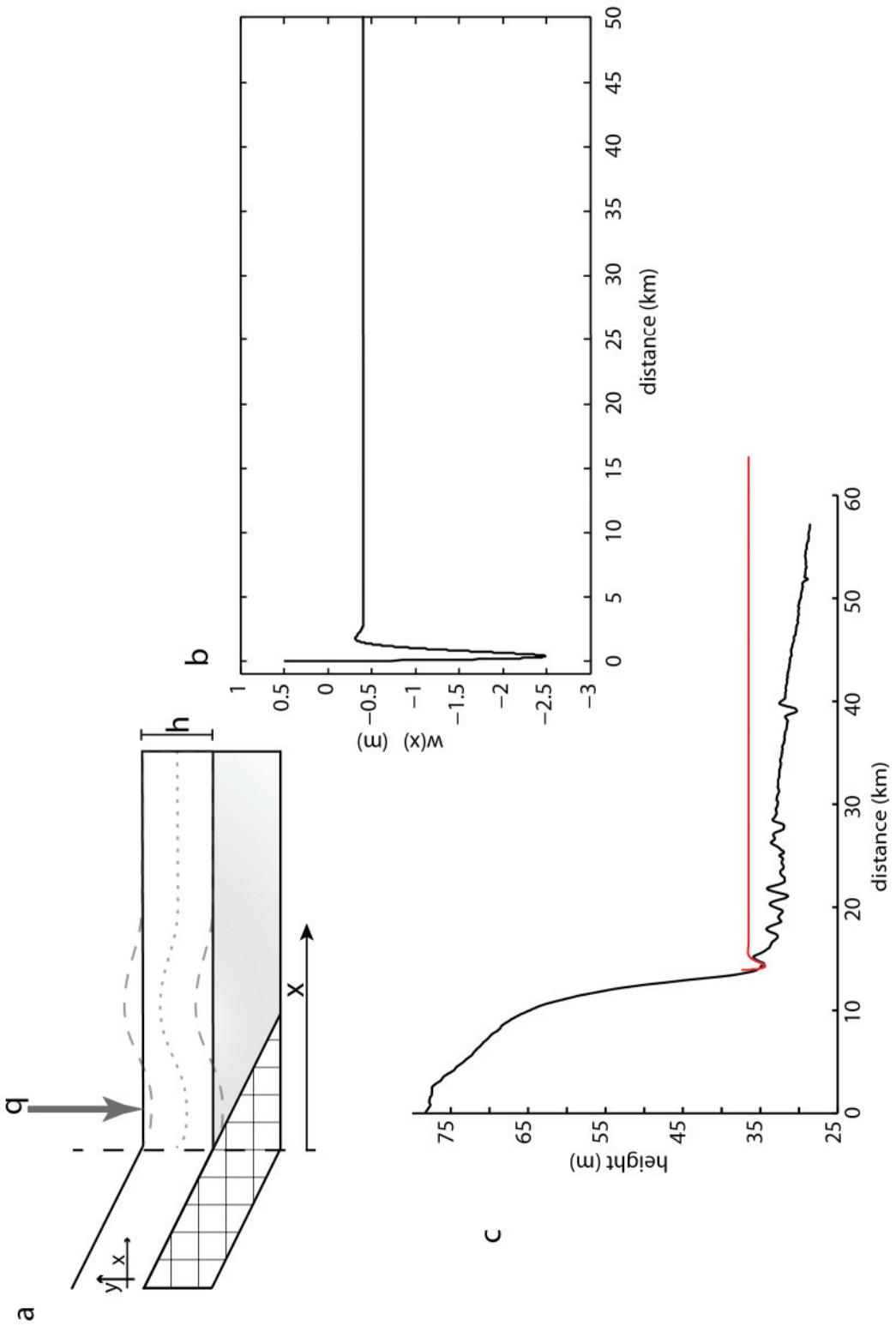
a
q
h
x
y
x
b
w(x) (m)
distance (km)
c
height (m)
distance (km)

Figure 22: a)- Force diagram modeling an elastic beam resting on split elastic foundation with a point load at the grounding line, length *L*, and thickness *h* (Sayag and Worster, 2011). b) Predicted profile of the KIS grounding line created from a) (6500x vertical exaggeration). c) Profile b) overlain on top of the kinematic GPS line K2(800x vertical exaggeration).

3.3 Pinch and swell structures

Folding theory examines the viscous deformation of layered materials undergoing a perturbation to the stress field caused by layer-parallel compression, extension, shear, or a density instability (Johnson and Fletcher, 1994; Schmalholz et al., 2008; Schmalholz et al., 2007). Viscous folding theory has been used to examine earth processes such as the folding of rock layers, isostatic rebound, and buckling instabilities in rock layers and ice shelves (Collins and Mccrae, 1985; Johnson and Fletcher, 1994; Smith, 1975). The layers may be treated as sets or as isolated layers depending on the magnitude of the viscosity contrast between layers. If the viscosity contrast is very large, such as between ice and air, the layer can be treated as a single isolated layer (Johnson and Fletcher, 1994).

Glacier ice deforms as a viscous fluid in response to gravitational driving stresses. A floating ice shelf has a much higher viscosity than the two bounding layers of air and water, allowing it to be treated as an isolated layer. Ice is a slightly nonlinear material whose behavior is described by Nys's generalization of Glen's Flow Law in which the strain rates $\dot{\epsilon}_{jk}$ are dependent on the deviatoric stresses τ_{jk} following

$$\dot{\epsilon}_{jk} = A\tau_E^{m-1}\tau_{jk} \quad \textbf{(25)}$$

with A representing a creep parameter, τ_E the effective stress, and m the ratio between shear and normal viscosity where $m = \frac{\mu_s}{\mu_n} = 3$ (Cuffey and Paterson, 2010). Ice is a strain-rate softening material in which the effective viscosity decreases as strain rate increases, allowing the ice to deform more readily. In non-linear materials such as ice, perturbations in the stress field have been shown to amplify creating structures such as buckling or necking (Collins and Mccrae, 1985; Johnson and Fletcher, 1994; Ng and Conway, 2004; Smith, 1975).

When a homogenous nonlinear fluid deforming by pure shear undergoes a perturbation, a discontinuity in the horizontal normal stress is created. The initial primary flow $\bar{\psi}$ combined with the secondary flow $\tilde{\psi}$

$$\psi = \bar{\psi} + \tilde{\psi} \quad \textbf{(26)}$$

creates a deflection of the top and bottom interfaces of the fluid (Figure 23). The direction of deflection depends upon the sign of the stress acting on the fluid. If the fluid is being compressed the interfaces between layers deflect in the same direction and folding occurs. When the fluid is stretching, the interfaces deflect in opposite directions and pinch and swell structures form.

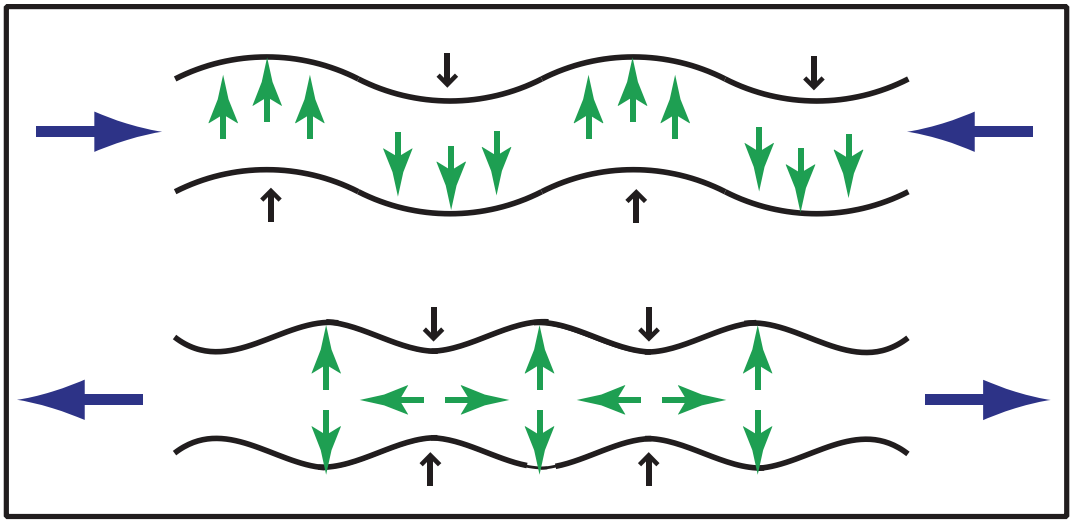

Figure 23: Diagram of the deflection of the interfaces forming either folding (top) or pinch and swell (bottom) structures. Blue arrows depict direction of strain either compression (top) or extension (bottom).

The following analysis assumes an ice shelf of thickness *h,* with parallel interfaces for the top and bottom, that is deforming under plane strain where $\epsilon_{xz} = \epsilon_{xz} = \epsilon_{yy} = 0$. Mean velocity components for the primary flow are

$$\bar{v}_x = \dot{\epsilon}_{xx} x \tag{27}$$

$$\bar{v}_z = -\dot{\epsilon}_{xx} z \tag{28}$$

in which the over bar represents a mean quantity. The fluid motion for the perturbed flow can be described using the Navier-Stokes equations for plane strain ,simplified for creep flow

$$(2\mu_n - \mu_s)\left(\frac{\partial^2 \tilde{v}_x}{\partial x^2}\right) + \mu_s\left(\frac{\partial^2 \tilde{v}_x}{\partial z^2}\right) = \frac{\partial \tilde{P}}{\partial x} \tag{29}$$

$$(2\mu_n - \mu_s)\left(\frac{\partial^2 \tilde{v}_z}{\partial z^2}\right) + \mu_s\left(\frac{\partial^2 \tilde{v}_z}{\partial x^2}\right) = \frac{\partial \tilde{P}}{\partial z} \quad \textbf{(30)}$$

in which the tilde represents a mean quantity and $\tilde{P}$ represents mean pressure (Johnson and Fletcher, 1994). Introducing the stream function to represent the perturbed velocity components, $\tilde{v}_x = -\frac{\partial \psi}{\partial z}$ and $\tilde{v}_z = \frac{\partial \psi}{\partial x}$, simplifies equations (29) and (30) to

$$\frac{\partial^4 \psi}{\partial x^4} + 2(2V - 1)\left(\frac{\partial^4 \psi}{\partial x^2 \partial z^2}\right) + \left(\frac{\partial^4 \psi}{\partial z^4}\right) = 0 \quad \textbf{(31)}$$

in which $V = m^{-1}$ for a power law fluid (Johnson and Fletcher, 1994). Using the stream function

$$\psi = \frac{1}{l} W \sin(lx) \quad \textbf{(32)}$$

in which $l = 2\pi L$ and W is a function of z and substituting (32) into equation (31) creates

$$\frac{d^4 W}{dz^4} - 2(2V - 1)l^2\left(\frac{d^2 W}{dz^2}\right) + W l^4 = 0 \quad \textbf{(33)}$$

The general solution for the velocity potential for a power law fluid becomes

$$\psi = \left(\frac{1}{l}\right)[a\cos(\alpha lz)\cosh(\beta lz) + b\sin(\alpha lz)\sinh(\beta lz) + c\cos(\alpha lz)\sinh(\beta lz) + d\sin(\alpha lz)\cosh(\beta lz)]\sin(lx) \quad (34)$$

with constants $\beta = \sqrt{\frac{1}{m}}$ and $\alpha = \sqrt{\frac{(m-1)}{m}}$ related to the viscosity of the ice (Johnson and Fletcher, 1994). In pinch and swell cases, the constants *a* and *b* are equal to zero since they are associated to buckling. Setting the boundary stresses equal to zero for an isolated layer produces

$$c = \frac{-d\sin(\alpha k)\sinh(\beta k)}{\cos(\alpha k)\cosh(\beta k)} \quad (35)$$

and

$$d = \frac{\dot{\epsilon}_{xx}\left(\frac{\mu_s}{\mu_n}\right)2A\cos(\alpha k)\cosh(\beta k)}{\left[\left(\frac{\alpha}{\beta}\right)\sinh(\beta k)\cosh(\beta k) + \sin(\alpha k)\cos(\alpha k)\right]} \quad (36)$$

in which the dimensionless wave number

$$k = \frac{\pi \mathrm{h}}{\lambda} \quad (37)$$

depends on the wavelength λ, and the thickness *h*, of the ice. An instability will amplify at the rate of

$$\frac{dA}{dt} = -(1+Q)\dot{\epsilon}_{xx}A_o \quad (38)$$

in which A_o is the amplitude of the original instability. The amplification factor q

$$Q = \frac{-2\left(\frac{\mu_s}{\mu_n}\right)}{1 + \left(\frac{\alpha}{\beta}\right)\left(\frac{\sinh(2\beta k)}{\sin(2\alpha k)}\right)} \quad \textbf{(39)}$$

depends on the material properties (Johnson and Fletcher, 1994). Instabilities can amplify for any materials with $m \geq 1$. For the case of $m = 3$, such as ice, $Q < -1$, making the wavelength to thickness ratio 2.19 or greater, for instabilities to amplify (Figure 24). The maximum value for Q is -3 for any combination of wavelength to thickness ratio (Figure 24).

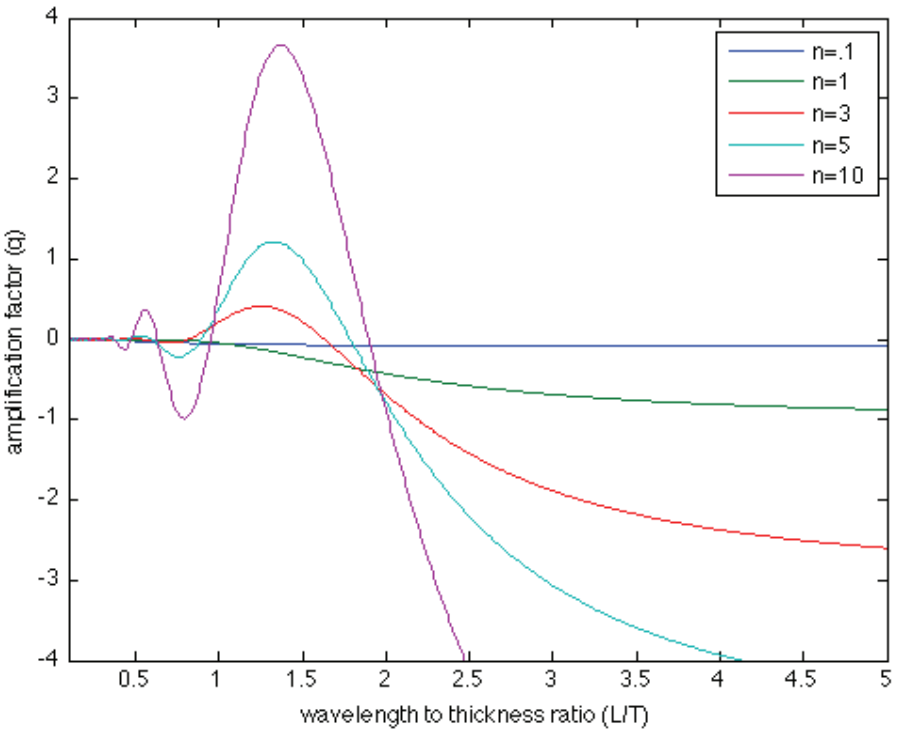

Figure 24: Graph of the wavelength to thickness ratio vrs amplification factor q for isolated power law materials with viscosity ratios from 0.1 to 10 (Johnson and Fletcher, 1994).

The amplification factor, and thus $\frac{dA}{dt}$, is sensitive to the ratio k. For example, holding all other values constant ($\dot{\epsilon}_{xx} = 2.9\ x\ 10^{-3}$ a $^{-1}$, $A_o = 40$ m, and $\lambda = 1.3$ km) a less than 10% change in the thickness from 550 m to 500 meters will double the amplification rate from 0.03 ma^{-1} to 0.06 ma^{-1}. The initial amplitude used here is the tilt in ice as it transitions from grounded to floating and the strain rate is the average strain rate measured across the grounding line (Figure 6, Figure 27). Using the maximum value for the amplification factor ($q = -3$), the approximate maximum rate of amplification for the region is 0.23 ma^{-1}.

Some of the terms in equations (38) and (39) are better constrained than others. Ice thicknesses along the grounding line are not known to the precision needed to create a definitive model of the rate of amplification for the region. Ice thickness is from the BEDMAP dataset, which has a data point every 5 km. The thickness data from BEDMAP appear to be about 40 m larger than those estimated from radar profiles suggesting imprecision in the dataset on the scales needed to constrain the calculation further. The variability in thickness as well as density, wavelength, and strain rate leads to range of possible solutions for the rate of amplification. One solution that uses the BEDMAP dataset for the thickness of the ice, an average wavelength of the features, and an average strain rate over the grounding line predicts the amplification rate to range from 0.0 ma^{-1} to 0.06 ma^{-1} across the region (Figure 25). The calculation for Figure 25 has a strain rate of 7.46 x 10^{-4} for areas approximately 20 km past the grounding line and then a zero strain

rate further than that. The nonlinear rheology of the ice combined with the stretching occurring across the grounding line leads to the amplification of instabilities within the ice (Figure 25).

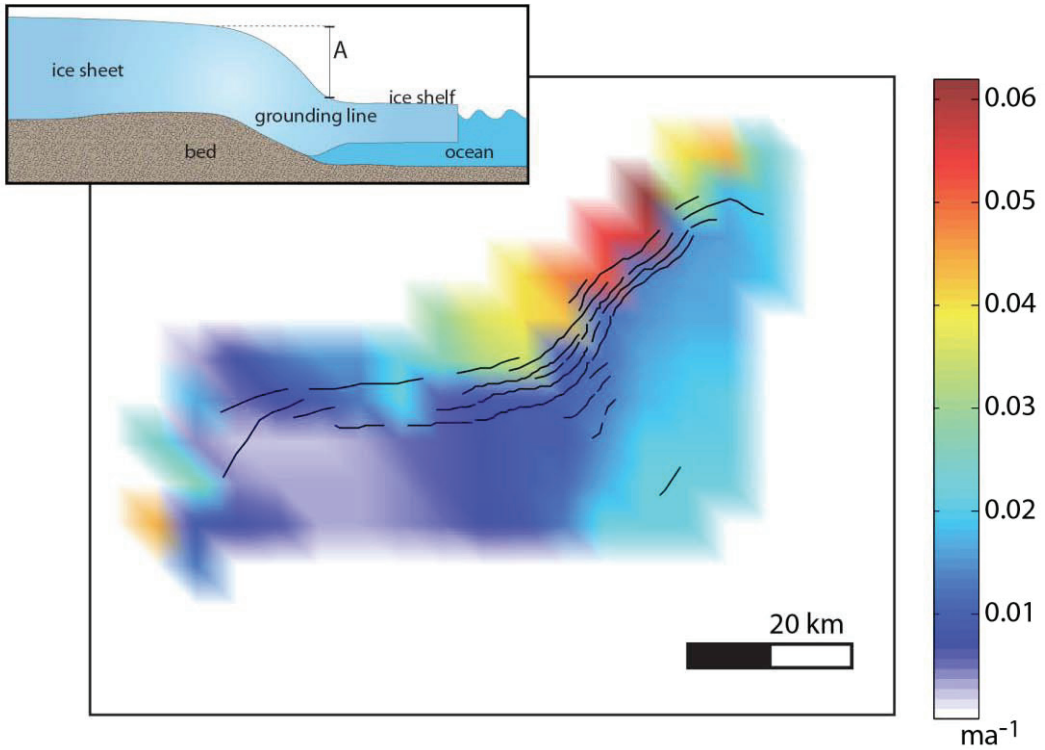

Figure 25: Diagram of the amplitude of tilt in layer of ice at grounded to floating transition (top) and calculated rate of amplification for KIS grounding line.

3.3.1 Relaxation rate

If the features moved out the area of active formation, the rate at which the surface will subside is (Johnson and Fletcher, 1994)

$$\frac{dr}{dt} = \frac{-\rho_i g L A}{4\pi\mu} \quad \textbf{(40)}$$

in which all variables are as defined in previous sections and viscosity is defined to be at the plastic limit with a value on the order of 10^{14} Pa s (Cuffey and Paterson, 2010). Features with larger amplitudes will decay more quickly than those with smaller amplitudes. For features with the amplitudes of 3 m, the relaxation rate would be approximately 0.8 ma^{-1} , suggesting that surface undulations would not persist long after the initial formation.

4 Conclusion and Discussion

Downstream of the KIS grounding line, there exists a set of shore-parallel long wavelength surface undulations exist that do not appear at neighboring grounding lines (Figure 3). These features have amplitudes approximately 0.5 to 3.0 m and wavelengths of approximately 1.3 km (Figure 7). While the features are all of similar scale, they are not uniformly distributed nor are their geometries uniform (Figure 5, Figure 6). Although regions with abundant basal crevasses do correspond to some of the areas with lower surface elevation, the relationship is not simple and does not explain the observed surface undulations (Figure 9, Figure 10). Repeat observations show that the features are fixed relative to the grounding line and tide height on timescales up to a few years. That is, they do not appear to be an excitation of the material due to tidal motion (Figure 11, Figure 12, Figure 13).

The KIS and WIS grounding line transitions have very different velocities and strain rates. Across the KIS strain grid, the surface velocities are measured at 0.04 ± 0.03 ma^{-1} to 7.37 ± 0.11 ma^{-1} with the slowest poles located in the grounded ice (Figure 14) (Appendix A). Comparatively, the neighboring WIS strain grid velocities were measured at $369.22 \pm .06$ ma^{-1} to $371.18 \pm .05$ ma^{-1} (Figure 14) (Appendix B). These measurements highlight the difference between KIS and other grounding line settings with fast flowing ice. Because the transition at the grounding line of KIS is that of stagnant grounded ice to floating, the principle extensive strain rates calculated within the KIS strain grid ($6.00 \times 10^{-6} \pm 1.12 \times 10^{-3}$ to $5.80 \times 10^{-3} \pm 2.14 \times$

10^{-4} with a mean of $1.00 \times 10^{-3} \pm 5.65 \times 10^{-4}$) are higher than those observed within the neighboring WIS strain grid ($7.83 \times 10^{-5} \pm 6.90 \times 10^{-7}$ to $8.01 \times 10^{-4} \pm 3.70 \times 10^{-7}$ with a mean of $4.87 \times 10^{-4} \pm 6.65 \times 10^{-7}$)(Figure 16, Figure 17, Figure 18) (Appendix F, Appendix G). The highest strain rates for both ice streams are located directly across the grounding line (Figure 17, Figure 18).

Elastic deformation is insufficient to describe the surface undulations observed at the grounding line of KIS. The elastic model based on a thin clamped plate describes an overall deflection of the surface but does not predict any undulations to the surface (Figure 20). The two point load models used here to evaluate bending at the grounding line produce a single undulation in the surface, a dip immediately downstream of the grounding-to-floating transition. Different treatments of the material properties yield slightly different geometries, longer and shorter wavelengths, but do not produce more than one undulation. Thus, something more than elastic properties of the ice must be responsible for the features observed at the KIS grounding line.

Viscous folding theory describes the deformation that occurs to a viscous layer that experiences extension or compression, such as the stretching of the ice over the grounding line. As long as the wavelength to thickness ratio of the ice remained above 2.19, which for example could be a wavelength of 1.3 km and a thickness of 594 m, instabilities created by the transition from grounded –to-floating ice can be amplified within a viscous layer (Figure 24). One possible model

of the current grounding line settings predicts amplification rates from 0 to 0.06 ma^{-1} (Figure 25). These results are supported by observations of viscous bucking features on both the RIS and George VI Ice Shelf in West Antarctica (Collins and Mccrae, 1985; LaBarbera and MacAyeal, 2011).

KIS became stagnant about 165 years ago (Catania et al., 2006). Changing from a transition like the one at WIS to one with stagnate ice before the grounding line and faster flowing ice downstream on the ice shelf, would have created a higher strain rate across the grounding line than existed before the stagnation. It is reasonable to assume that the strain rate has remained at the same magnitude observed today. If the features have continued to form since the stagnation of KIS 165 years ago, the current amplification rates would create surface undulations with amplitudes from 0 to 9.9 m. The observed surface features have approximate amplitudes of 0 to 3.0 m which falls within the possible range predicted by viscous theory (Figure 7). This work determines that the elastic models are insufficient to explain the observations. It is thus determined that the surface undulations downstream of the KIS grounding line are not derived from an elastic process but are viscous in origin. This determination suggests that the grounding line transition may be more appropriately described using a viscous approach rather than an elastic model.

References

Alley, R.B., and Bindschadler, R.A., 2001, The West Antarctic Ice Sheet and sea-level change, *in* The West Antarctic Ice Sheet Behavior and Environment, American Geophysical Union, Washington, D.C., p. 1-11.

Anandakrishnan, S., and Alley, R.B., 1997, Tidal forcing of basal seismicity of ice stream C , West Antarctica , observed far inland: Journal of Geophysical Research, , no. 102, p. 15.

Bindschadler, R., Bamber, J., and Anandakrishnan, S., 2001, Onset of streaming flow in the Siple Coast region, West Antarctica, *in* The West Antarctic Ice Sheet Behavior and Environment, American Geophysical Union, Washington, D.C., p. 123-136.

Le Brocq, A.M., Payne, A.J., and Vieli, A., 2010, An improved Antarctic dataset for high resolution numerical ice sheet models (ALBMAP v1): Earth System Science Data, v. 2, no. 2, p. 247-260, doi: 10.5194/essd-2-247-2010.

Brunt, K.M., Fricker, H. a., Padman, L., Scambos, T. a., and O'Neel, S., 2010, Mapping the grounding zone of the Ross Ice Shelf, Antarctica, using ICESat laser altimetry: Annals of Glaciology, v. 51, no. 55, p. 71-79, doi: 10.3189/172756410791392790.

Cai, J., Wang, J., Wu, J., Hu, C., Grafarend, E., and Chen, J., 2008, Horizontal Deformation Rate Analysis Based on Multiepoch GPS Measurements in Shanghai: Journal of Surveying Engineering, v. 134, no. 4, p. 132-137.

Catania, G.A., 2011, Personal Communication.

Catania, G. a., Neumann, T. a., and Price, S.F., 2008, Characterizing englacial drainage in the ablation zone of the Greenland ice sheet: Journal of Glaciology, v. 54, no. 187, p. 567-578, doi: 10.3189/002214308786570854.

Catania, G.A., Scambos, T.A., Conway, H., Raymond, C.F., Snow, N., and Sciences, S., 2006, The sequential stagnation of Kamb Ice Stream , West: Geophysical Research Letters, v. 33, no. L14502, p. 4, doi: 10.1029/2006GL026430.

Collins, I.F., and Mccrae, I.R., 1985, CREEP BUCKLING OF ICE SHELVES AND THE FORMATION OF: Journal of Glaciology, v. 31, no. 109, p. 242-252.

Cruikshank, K.M., 2012, Personal Communication.

Cuffey, K.M., and Paterson, W.S.B., 2010, The Physics of Glaciers: Elsevier Science, Burlington.

Durand, G., Gagliardini, O., de Fleurian, B., Zwinger, T., and Le Meur, E., 2009, Marine ice sheet dynamics: Hysteresis and neutral equilibrium: Journal of Geophysical Research, v. 114, no. F3, p. 1-10, doi: 10.1029/2008JF001170.

Fowler, C.M.R., 2005, The Solid Earth: An introduction to global geophysics: Cambridge University Press, New York.

Fricker, H.A., and Padman, L., 2006, Ice shelf grounding zone structure from ICESat laser altimetry: Geophysical Research Letters, v. 33, no. 15, doi: 10.1029/2006GL026907.

Garmin, 2008, GPS 18x Technical Specifications: , p. 33.

Holdsworth, G., 1969, Flexure of a floating ice tongue: Journal of Glaciology, v. 8, p. 385-397.

Johnson, A.M., and Fletcher, R.C., 1994, Folding of Viscous Layers: Columbia University Press, New York.

Joughin, I., Tulaczyk, S., Bindschadler, R., and Price, S.F., 2002, Changes in west Antarctic ice stream velocities: Observation and analysis: Journal of Geophysical Research, v. 107, no. B11, p. 1-22, doi: 10.1029/2001JB001029.

Kamb, B., 2001, Basal zone of the West Antarctic ice streams and its role in lubrication of their raid motion, *in* The West Antarctic Ice Sheet Behavior and Environment, American Geophysical Union, Washington, D.C., p. 157-199.

LaBarbera, C.H., and MacAyeal, D.R., 2011, Traveling supraglacial lakes on George VI Ice Shelf, Antarctica: Geophysical Research Letters, v. 38, no. 24, p. 1-5, doi: 10.1029/2011GL049970.

MacGregor, J. a., Anandakrishnan, S., Catania, G. a., and Winebrenner, D.P., 2011, The grounding zone of the Ross Ice Shelf, West Antarctica, from ice-penetrating radar: Journal of Glaciology, v. 57, no. 205, p. 917-928, doi: 10.3189/002214311798043780.

Mercer, J.H., 1978, West Antarctic ice sheet and CO2 greenhouse effect: a threat of disaster: Nature, v. 271, no. 5643, p. 321-325, doi: 10.1038/271321a0.

Ng, F., and Conway, H., 2004, Fast-flow signature in the stagnated Kamb Ice Stream, West Antarctica: Geology, v. 32, no. 6, p. 481-484, doi: 10.1130/G20317.1.

Padman, L., 2012, Personal Communication.

Reeh, N., Christensen, E.L., Mayer, C., and Olesen, O.B., 2003, Tidal bending of glaciers: a linear viscoelastic approach: Annals of Glaciology, v. 37, no. 1, p. 83-89, doi: 10.3189/172756403781815663.

Retzlaff, R., and Bentley, C.R., 1993, Timing of stagnation of Ice Stream C , West Antarctica , from short-pulse radar studies of buried surface crevasses: Journal of Glaciology, v. 39, no. 133, p. 553-561.

Robison, R. a. V., Huppert, H.E., and Worster, M.G., 2010, Dynamics of viscous grounding lines: Journal of Fluid Mechanics, v. 648, p. 363, doi: 10.1017/S0022112009993119.

Sayag, R., 2011, Personal Communication.

Sayag, R., and Worster, M.G., 2011, Elastic response of a grounded ice sheet coupled to a floating ice shelf.: Physical review. E, Statistical, nonlinear, and soft matter physics, v. 84, no. 3 Pt 2, p. 036111.

Scambos, T. a., Haran, T.M., Fahnestock, M. a., Painter, T.H., and Bohlander, J., 2007, MODIS-based Mosaic of Antarctica (MOA) data sets: Continent-wide surface morphology and snow grain size: Remote Sensing of Environment, v. 111, p. 242-257, doi: 10.1016/j.rse.2006.12.020.

Schmalholz, S.M., Schmid, D.W., and Fletcher, R.C., 2008, Evolution of pinch-and-swell structures in a power-law layer: Journal of Structural Geology, v. 30, no. 5, p. 649-663, doi: 10.1016/j.jsg.2008.01.002.

Schmalholz, S.M., Schmid, D.W., and Fletcher, R.C., 2007, Finite Amplitude Necking and Evolution of Pinch-and-Swell Structures in Power-Law Fluids: v. 9, p. 8529.
Schoof, C., 2007, Ice sheet grounding line dynamics: Steady states, stability, and hysteresis: Journal of Geophysical Research, v. 112, no. F3, p. 1-19, doi: 10.1029/2006JF000664.
Schoof, C., 2011, Marine ice sheet dynamics. Part 2. A Stokes flow contact problem: Journal of Fluid Mechanics, v. 679, p. 122-155, doi: 10.1017/jfm.2011.129.
Shabtaie, S., and Bentley, C.R., 1987, West Antarctic ice streams draining into the Ross Ice Shelf: configuration and mass balance: Journal of Geophysical Research, v. 92, no. B2, p. 1311-1336, doi: 10.1029/JB092iB02p01311.
Smith, R.B., 1975, Unified theory of the onset of folding, boudinage, and mullion structure: Geological Society of America Bulletin, v. 86, p. 1601-1609.
Turcotte, D.L., and Schubert, G., 2002, Geodynamics: Cambridge University Press, New York.
Vaughan, D.G., 1995, Tidal flexure at ice shelf margins.pdf: Journal of Geophysical Research, v. 100, no. B4, p. 6213-6224.
Weertman, J., 1974, STABILITY OF THE JUNCTION OF AN ICE SHEET AND AN ICE SHELF By].: Journal of Glaciology, v. 13, no. 67, p. 3-11.
Whillans, I.M., Bentley, C.R., and van der Veen, C.J., 2001, Ice streams B and C, *in* Alley, Richard B ;Bindschadler, R.A. ed., The West Antarctic Ice Sheet Behavior and Environment, American Geophysical Union, Washington, D.C., p. 257-281.

APPENDIX

A Kamb Ice Stream strain grid locations and velocities

Station locations in decimal degrees using WGS1984 in November and December of 2006 and 2007 along with calculated speeds, azimuths of direction, and associated speed error for grid network at ground line of KIS.

station name	latitude 2006	longitude 2006	latitude 2007	longitude 2007	Speed (ma-1)	Azimuth (°)	Speed error
KA1	82.864363	154.785463	82.864362	154.785469	0.10	-52.30	0.23
KA2	82.855548	154.770746	82.855548	154.770751	0.07	-36.40	0.21
KA3	82.846262	154.759492	82.846262	154.759496	0.05	-45.00	0.14
KA4	82.837413	154.746851	82.837412	154.746853	0.04	-68.90	0.03
KA5	82.828130	154.734428	82.828130	154.734431	0.06	-75.50	0.14
KA6	82.819387	154.723084	82.819386	154.723088	0.07	-63.30	0.20
KA7	82.810289	154.709919	82.810286	154.709637	3.86	160.40	0.07
KB1	82.862602	154.858001	82.862602	154.858012	0.15	-47.10	0.29
KB2	82.853643	154.841963	82.853643	154.841972	0.13	-38.70	0.17
KB3	82.844741	154.833363	82.844741	154.833371	0.11	-34.50	0.14
KB4	82.835385	154.817575	82.835384	154.817584	0.12	-41.30	0.13
KB5	82.825805	154.807898	82.825805	154.807906	0.13	-60.80	0.12
KB6	82.817193	154.792622	82.817192	154.792633	0.18	-60.70	0.15
KB7	82.807189	154.782744	82.807188	154.782762	0.30	-62.20	0.23
KC1	82.861172	154.930337	82.861171	154.930363	0.37	-41.00	0.25
KC2	82.852452	154.913914	82.852452	154.913937	0.32	-35.80	0.16
KC3	82.843350	154.904453	82.843350	154.904473	0.29	-35.00	0.18
KC4	82.833881	154.888223	82.833881	154.888242	0.26	-40.10	0.13
KC5	82.824089	154.878458	82.824088	154.878476	0.28	-50.10	0.18
KC6	82.816077	154.863566	82.816076	154.863589	0.36	-54.80	0.16
KC7	82.805611	154.853459	82.805606	154.853198	3.60	162.20*	0.10
KD1	82.859613	155.003312	82.859610	155.003078	3.19	159.90*	0.13
KD2	82.850723	154.987660	82.850722	154.987717	0.78	-32.70	0.24
KD3	82.841607	154.976431	82.841606	154.976481	0.69	-32.60	0.17
KD4	82.832210	154.961572	82.832209	154.961614	0.58	-34.70	0.15
KD5	82.822867	154.952303	82.822866	154.952344	0.61	-45.80	0.19
KD6	82.813934	154.932931	82.813931	154.932983	0.79	-49.90	0.16

station name	latitude 2006	longitude 2006	latitude 2007	longitude 2007	Speed (ma-1)	Azimuth (°)	Speed error
KD7	82.804897	154.925803	82.804892	154.925880	1.17	-51.10	0.28
KE1	82.857852	155.076170	82.857848	155.076308	1.92	-37.60	0.21
KE2	82.849253	155.060330	82.849248	155.060175	2.19	170.60*	0.10
KE3	82.840339	155.050982	82.840334	155.050821	2.26	169.20*	0.07
KE4	82.830482	155.032049	82.830481	155.032151	1.40	-31.40	0.15
KE5	82.821985	155.024093	82.821981	155.024198	1.48	-40.10	0.11
KE6	82.812923	155.003785	82.812917	155.003906	1.76	-45.10	0.17
KE7	82.803865	155.000190	82.803857	155.000347	2.29	-45.60	0.18
KF1	82.856314	155.148578	82.856307	155.148790	3.00	-41.00	0.12
KF2	82.847584	155.133644	82.847576	155.133855	2.98	-40.70	0.10
KF3	82.838663	155.121627	82.838656	155.121835	2.94	-41.00	0.08
KF4	82.828845	155.106304	82.828838	155.106495	2.72	-41.50	0.01
KF5	82.820354	155.099904	82.820347	155.100105	2.85	-41.20	0.08
KF6	82.811787	155.082598	82.811779	155.082811	3.04	-41.80	0.08
KF7	82.802750	155.070720	82.802740	155.070961	3.47	-43.50	0.09
KG1	82.854610	155.221170	82.854599	155.221432	3.73	-42.40	0.13
KG2	82.845984	155.205857	82.845974	155.206126	3.82	-42.00	0.12
KG3	82.836873	155.193796	82.836862	155.194073	3.94	-41.80	0.11
KG4	82.827397	155.176430	82.827387	155.176710	3.98	-41.30	0.10
KG5	82.818776	155.170588	82.818765	155.170879	4.15	-41.60	0.14
KG6	82.810846	155.153094	82.810834	155.153390	4.24	-42.10	0.08
KG7	82.801152	155.145579	82.801139	155.145897	4.56	-42.60	0.09
KH1	82.852921	155.293548	82.852908	155.293865	4.53	-42.80	0.15
KH2	82.844301	155.277819	82.844288	155.278140	4.59	-42.80	0.15
KH3	82.835088	155.266157	82.835074	155.266488	4.74	-42.80	0.17
KH4	82.825899	155.249841	82.825886	155.250174	4.77	-42.60	0.08
KH5	82.816904	155.242269	82.816890	155.242613	4.92	-42.50	0.09
KH6	82.808854	155.227335	82.808840	155.227685	5.02	-42.50	0.09
KH7	82.799508	155.216509	82.799493	155.216877	5.28	-42.40	0.09
KI1	82.851382	155.365738	82.851367	155.366108	5.28	-42.90	0.21
KI2	82.842699	155.351277	82.842683	155.351655	5.41	-42.80	0.11

station name	latitude 2006	longitude 2006	latitude 2007	longitude 2007	Speed (ma-1)	Azimuth (°)	Speed error
KI3	82.833355	155.339381	82.833339	155.339770	5.56	-42.70	0.09
KI4	82.824380	155.323992	82.824364	155.324387	5.65	-42.50	0.18
KI5	82.815674	155.313650	82.815658	155.314051	5.75	-42.40	0.09
KI6	82.806658	155.300693	82.806642	155.301105	5.90	-42.30	0.10
KI7	82.797913	155.290383	82.797896	155.290812	6.15	-41.90	0.10
KJ1	82.849728	155.439136	82.849711	155.439557	6.02	-43.00	0.11
KJ2	82.840986	155.423525	82.840968	155.423954	6.14	-42.90	0.10
KJ3	82.831616	155.411912	82.831599	155.412349	6.27	-42.70	0.10
KJ4	82.822552	155.394394	82.822534	155.394836	6.32	-42.40	0.12
KJ5	82.814609	155.386340	82.814591	155.386788	6.42	-42.40	0.13
KJ6	82.804990	155.372161	82.804972	155.372622	6.60	-42.10	0.12
KJ7	82.796517	155.360636	82.796499	155.361109	6.78	-41.90	0.10
KK1	82.848383	155.510466	82.848364	155.510932	6.67	-43.00	0.13
KK2	82.839372	155.496990	82.839353	155.497466	6.82	-42.90	0.09
KK3	82.830207	155.481631	82.830187	155.482113	6.91	-42.70	0.07
KK4	82.821138	155.470652	82.821119	155.471139	6.97	-42.40	0.01
KK5	82.811953	155.461992	82.811933	155.462485	7.07	-42.20	0.12
KK6	82.803012	155.446345	82.802992	155.446851	7.25	-41.80	0.10
KK7	82.794326	155.430246	82.794307	155.430761	7.37	-41.60	0.11

* Station velocities were *******

B Whillans Ice Stream strain grid location and velocities

Station names and locations in decimal degrees using WGS1984 projection for the field seasons 2006 and 2007, along with speeds (ma^{-1}) and azimuth of direction (degrees) with associated speed error (ma^{-1}) for the grid network at the grounding line of WIS.

station name	latitude 2006	longitude 2006	latitude 2007	longitude 2007	Speed (ma^{-1})	Azimuth (°)	Speed error
WA2	84.397507	165.103224	84.396068	165.134668	369.27	-40	0.018
WA3	84.406015	165.143908	84.404573	165.175393	369.34	-40	0.048
WA4	84.414217	165.183469	84.412773	165.214975	369.22	-40	0.06
WB1	84.383598	165.149647	84.382155	165.180997	369.28	-40	0.055
WB2	84.392866	165.184837	84.391423	165.216245	369.4	-40	0.043
WB3	84.402759	165.244780	84.401311	165.276230	369.44	-40	0.056
WB4	84.408617	165.259341	84.407168	165.290812	369.4	-40	0.074
WC1	84.379790	165.233978	84.378346	165.265303	369.32	-40	0.063
WC2	84.388967	165.264958	84.387519	165.296332	369.45	-40	0.054
WC3	84.399625	165.330614	84.398173	165.362030	369.48	-40	0.069
WC4*	84.404258	165.339295	84.402815	165.370956	NaN	NaN	NaN
WD1	84.375703	165.319453	84.374253	165.350775	369.76	-39.9	0.066
WD2	84.384969	165.347010	84.383518	165.378362	369.6	-39.9	0.065
WD3	84.396180	165.419758	84.394724	165.451154	369.67	-40	0.123
WD4*	84.400423	165.423486	84.398972	165.455081	NaN	NaN	NaN
WE1	84.371847	165.405058	84.370395	165.436367	369.96	-39.9	0.066
WE2	84.381531	165.431746	84.380076	165.463112	370.12	-39.9	0.06
WE3*	84.392454	165.508728	84.390994	165.540254	NaN	NaN	NaN
WE4	84.396993	165.505385	84.395534	165.536792	369.88	-39.9	0.11
WF1*	84.368220	165.488648	84.366762	165.520082	NaN	NaN	NaN
WF2	84.377649	165.515996	84.376191	165.547355	370.43	-39.9	0.021
WF3	84.388632	165.595322	84.387167	165.626711	370.4	-39.9	0.094
WF4	84.393285	165.590851	84.391821	165.622255	370.26	-39.9	0.064
WG1	84.364396	165.580090	84.362944	165.611358	369.95	-39.7	0.063
WG2	84.374538	165.601267	84.373079	165.632583	370.18	-39.8	0.036

station name	latitude 2006	longitude 2006	latitude 2007	longitude 2007	Speed (ma^{-1})	Azimuth (°)	Speed error
WG3	84.384525	165.677932	84.383059	165.709281	370.27	-39.8	0.053
WG4	84.389640	165.681325	84.388173	165.712692	370.25	-39.9	0.06
WH1*	84.360971	165.665295	84.359518	165.696597	NaN	NaN	NaN
WH2*	84.370951	165.683325	84.369492	165.714620	NaN	NaN	NaN
WH3	84.380531	165.757497	84.379064	165.788834	370.42	-39.8	0.064
WH4	84.386146	165.773097	84.384677	165.804456	370.44	-39.8	0.088
WI1	84.357561	165.746813	84.356103	165.778080	370.57	-39.6	0.129
WI2	84.367141	165.765783	84.365680	165.797083	370.57	-39.7	0.062
WI3	84.375820	165.839865	84.374353	165.871199	370.68	-39.7	0.064
WI4	84.382944	165.857672	84.381474	165.889030	370.67	-39.7	0.09
WJ1	84.353659	165.830072	84.352200	165.861332	370.8	-39.5	0.058
WJ2	84.362238	165.866801	84.360775	165.898099	370.91	-39.6	0.053
WJ3	84.370377	165.907598	84.368910	165.938921	370.86	-39.6	0.064
WJ4	84.378517	165.946882	84.377047	165.978229	370.83	-39.6	0.097
WK1	84.349553	165.909412	84.348093	165.940667	371.02	-39.5	0.065
WK2	84.358781	165.951798	84.357317	165.983093	371.09	-39.5	0.041
WK3	84.366303	165.991869	84.364835	166.023187	371.07	-39.5	0.046
WK4	84.374435	166.031482	84.372965	166.062826	371.01	-39.5	0.077
WL1	84.346186	165.989550	84.344726	166.020801	371.18	-39.4	0.048
WL2	84.355043	166.036584	84.353579	166.067871	371.22	-39.4	0.023
WL3	84.363039	166.074278	84.361571	166.105592	371.22	-39.4	0.049
WL4	84.370359	166.111406	84.368889	166.142745	371.16	-39.4	0.058

* Stations that were damaged.

C Kamb Ice Stream strain components

Stations Used	$\dot{\epsilon}_{xx}$	$\dot{\epsilon}_{xy}$	$\dot{\epsilon}_{yx}$	$\dot{\epsilon}_{yy}$	$\dot{\epsilon}_{xx}$ er.	$\dot{\epsilon}_{xy}$ er	$\dot{\epsilon}_{yx}$ er	$\dot{\epsilon}_{yy}$ er
KA1 KA2 KB1 KB2	5.7E-5	7.3E-6	-4.8E-5	-4.5E-5	5.1E-6	5.0E-6	-6.4E-6	-6.5E-6
KA2 KA3 KB2 KB3	5.7E-5	1.5E-5	-3.8E-5	-1.1E-5	3.8E-6	3.6E-6	-4.6E-6	-4.3E-6
KA3 KA4 KB3 KB4	7.7E-5	1.6E-5	-3.9E-5	8.9E-6	2.7E-6	2.6E-6	-2.9E-6	5.1E-7
KA4 KA5 KB4 KB5	7.7E-5	1.5E-5	-6.1E-5	2.8E-5	2.7E-6	2.4E-6	-2.8E-6	2.5E-6
KA5 KA6 KB5 KB6	6.7E-5	-3.1E-5	-9.7E-5	4.2E-5	3.9E-6	-3.8E-6	-4.2E-6	4.0E-6
KA6 KA7 KB6 KB7	2.5E-3	2.2E-3	-1.1E-3	-7.8E-4	9.0E-6	2.9E-6	-6.7E-6	-6.1E-7
KB1 KB2 KC1 KC2	2.0E-4	1.8E-5	-1.4E-4	-5.9E-5	5.1E-6	5.0E-6	-6.2E-6	-6.4E-6
KB2 KB3 KC2 KC3	1.9E-4	2.0E-5	-1.3E-4	-2.4E-5	4.0E-6	3.6E-6	-4.5E-6	-4.2E-6
KB3 KB4 KC3 KC4	1.6E-4	2.1E-5	-1.2E-4	1.3E-5	3.8E-6	3.4E-6	-3.9E-6	3.6E-6
KB4 KB5 KC4 KC5	1.4E-4	2.7E-5	-1.2E-4	4.2E-5	3.6E-6	3.0E-6	-3.8E-6	3.3E-6
KB5 KB6 KC5 KC6	1.4E-4	-3.9E-5	-1.4E-4	9.0E-5	3.8E-6	-4.0E-6	-4.2E-6	4.5E-6
KB6 KB7 KC6 KC7	-2.2E-3	1.8E-3	7.7E-4	-6.6E-4	-4.0E-6	1.1E-6	1.6E-6	2.5E-7
KC1 KC2 KD1 KD2	-1.7E-3	-2.3E-3	6.7E-4	9.3E-4	-2.3E-6	-3.5E-6	8.0E-7	9.6E-7
KC2 KC3 KD2 KD3	4.6E-4	6.1E-5	-2.7E-4	-4.4E-5	5.3E-6	4.3E-6	-5.5E-6	-4.8E-6
KC3 KC4 KD3 KD4	3.8E-4	8.3E-5	-2.2E-4	-2.2E-5	4.4E-6	3.7E-6	-4.4E-6	-1.2E-7
KC4 KC5 KD4 KD5	3.1E-4	4.1E-5	-2.3E-4	8.5E-5	4.3E-6	3.6E-6	-4.4E-6	3.9E-6
KC5 KC6 KD5 KD6	3.4E-4	-7.6E-5	-3.4E-4	1.7E-4	4.8E-6	-4.6E-6	-5.1E-6	5.2E-6
KC6 KC7 KD6 KD7	2.6E-3	1.7E-3	-1.4E-3	-5.3E-4	9.0E-6	2.5E-7	-7.2E-6	1.3E-6
KD1 KD2 KE1 KE2	1.1E-3	1.1E-4	-9.2E-4	-4.2E-5	4.2E-7	-5.9E-7	-7.7E-7	4.6E-7
KD2 KD3 KE2 KE3	-3.3E-3	8.2E-5	9.3E-4	-7.1E-5	-7.4E-6	3.3E-6	4.8E-6	-3.8E-6

Stations Used	$\dot{\epsilon}_{xx}$	$\dot{\epsilon}_{xy}$	$\dot{\epsilon}_{yx}$	$\dot{\epsilon}_{yy}$	$\dot{\epsilon}_{xx}$ er.	$\dot{\epsilon}_{xy}$ er	$\dot{\epsilon}_{yx}$ er	$\dot{\epsilon}_{yy}$ er
KD3 KD4 KE3 KE4	-1.2E-3	-1.9E-3	2.1E-4	6.4E-4	8.1E-8	-1.3E-6	-5.9E-7	1.5E-10
KD4 KD5 KE4 KE5	8.7E-4	7.1E-5	-5.6E-4	2.0E-4	5.3E-6	3.6E-6	-4.9E-6	4.0E-6
KD5 KD6 KE5 KE6	8.6E-4	-1.3E-4	-6.9E-4	3.0E-4	5.2E-6	-4.1E-6	-5.2E-6	4.9E-6
KD6 KD7 KE6 KE7	9.4E-4	-3.4E-4	-8.0E-4	4.0E-4	6.4E-6	-5.2E-6	-6.8E-6	6.1E-6
KE1 KE2 KF1 KF2	3.1E-3	2.4E-3	-1.9E-3	-1.0E-3	5.0E-6	6.6E-6	-5.0E-6	-5.2E-6
KE2 KE3 KF2 KF3	5.5E-3	6.2E-5	-2.9E-3	-4.8E-5	4.5E-6	1.9E-6	-3.7E-6	-2.3E-6
KE3 KE4 KF3 KF4	3.3E-3	-1.9E-3	-2.1E-3	5.9E-4	3.6E-6	-2.6E-6	-3.4E-6	1.4E-6
KE4 KE5 KF4 KF5	1.1E-3	-2.7E-5	-1.2E-3	1.9E-4	3.1E-6	1.1E-6	-3.4E-6	2.6E-6
KE5 KE6 KF5 KF6	1.1E-3	-1.6E-4	-9.6E-4	2.9E-4	3.6E-6	-2.9E-6	-3.7E-6	3.6E-6
KE6 KE7 KF6 KF7	1.1E-3	-3.6E-4	-8.8E-4	4.4E-4	4.2E-6	-3.4E-6	-4.3E-6	4.0E-6
KF1 KF2 KG1 KG2	6.5E-4	-4.8E-5	-7.1E-4	1.2E-5	3.2E-6	-2.8E-7	-3.9E-6	2.6E-7
KF2 KF3 KG2 KG3	8.0E-4	-3.3E-5	-8.1E-4	3.4E-5	2.8E-6	-3.8E-7	-3.5E-6	4.1E-7
KF3 KF4 KG3 KG4	1.0E-3	7.3E-5	-9.5E-4	-7.2E-5	2.3E-6	-6.8E-7	-2.6E-6	7.5E-7
KF4 KF5 KG4 KG5	1.2E-3	-1.4E-4	-1.1E-3	1.3E-4	3.2E-6	-2.1E-6	-3.3E-6	2.2E-6
KF5 KF6 KG5 KG6	1.1E-3	-1.1E-4	-1.0E-3	1.6E-4	3.6E-6	-2.7E-6	-3.8E-6	3.1E-6
KF6 KF7 KG6 KG7	1.0E-3	-2.7E-4	-9.0E-4	3.5E-4	2.6E-6	-2.0E-6	-2.9E-6	2.4E-6
KG1 KG2 KH1 KH2	6.8E-4	-7.5E-5	-6.9E-4	5.4E-5	3.8E-6	-3.3E-6	-4.5E-6	4.0E-6
KG2 KG3 KH2 KH3	6.6E-4	-1.3E-4	-7.1E-4	1.0E-4	3.7E-6	-3.1E-6	-4.4E-6	3.8E-6
KG3 KG4 KH3 KH4	6.5E-4	-5.0E-5	-7.2E-4	6.0E-6	3.1E-6	-2.6E-6	-3.6E-6	3.0E-6
KG4 KG5 KH4 KH5	6.4E-4	-1.4E-4	-7.1E-4	1.4E-4	3.1E-6	-2.5E-6	-3.4E-6	2.7E-6
KG5 KG6 KH5 KH6	6.6E-4	-8.1E-5	-6.9E-4	1.1E-4	3.1E-6	-2.8E-6	-3.5E-6	3.2E-6

Stations Used	$\dot{\epsilon}_{xx}$	$\dot{\epsilon}_{xy}$	$\dot{\epsilon}_{yx}$	$\dot{\epsilon}_{yy}$	$\dot{\epsilon}_{xx}$ er.	$\dot{\epsilon}_{xy}$ er	$\dot{\epsilon}_{yx}$ er	$\dot{\epsilon}_{yy}$ er
KG6 KG7 KH6 KH7	6.7E-4	-2.3E-4	-6.3E-4	2.4E-4	2.5E-6	-2.0E-6	-2.9E-6	2.4E-6
KH1 KH2 KI1 KI2	6.9E-4	-8.8E-5	-6.5E-4	7.9E-5	4.1E-6	-3.7E-6	-4.8E-6	4.5E-6
KH2 KH3 KI2 KI3	7.3E-4	-1.4E-4	-6.7E-4	1.2E-4	3.6E-6	-3.0E-6	-4.0E-6	3.4E-6
KH3 KH4 KI3 KI4	7.5E-4	-6.6E-5	-6.8E-4	3.8E-5	3.5E-6	-3.1E-6	-3.9E-6	3.5E-6
KH4 KH5 KI4 KI5	7.6E-4	-1.2E-4	-6.8E-4	9.2E-5	3.0E-6	-2.6E-6	-3.4E-6	3.1E-6
KH5 KH6 KI5 KI6	7.8E-4	-1.2E-4	-6.9E-4	1.0E-4	2.7E-6	-2.3E-6	-3.1E-6	2.8E-6
KH6 KH7 KI6 KI7	8.0E-4	-2.5E-4	-6.8E-4	1.9E-4	2.7E-6	-2.3E-6	-3.1E-6	2.6E-6
KI1 KI2 KJ1 KJ2	6.5E-4	-1.2E-4	-6.2E-4	1.0E-4	3.5E-6	-3.2E-6	-4.1E-6	3.8E-6
KI2 KI3 KJ2 KJ3	6.4E-4	-1.3E-4	-6.0E-4	9.4E-5	2.8E-6	-2.3E-6	-3.0E-6	2.5E-6
KI3 KI4 KJ3 KJ4	6.4E-4	-8.6E-5	-5.7E-4	4.2E-5	3.5E-6	-3.0E-6	-3.8E-6	3.3E-6
KI4 KI5 KJ4 KJ5	6.1E-4	-9.4E-5	-5.4E-4	7.8E-5	3.6E-6	-3.3E-6	-4.1E-6	3.8E-6
KI5 KI6 KJ5 KJ6	6.2E-4	-1.6E-4	-5.4E-4	1.1E-4	3.1E-6	-2.6E-6	-3.6E-6	3.0E-6
KI6 KI7 KJ6 KJ7	6.3E-4	-2.3E-4	-5.4E-4	1.5E-4	3.0E-6	-2.6E-6	-3.5E-6	3.2E-6
KJ1 KJ2 KK1 KK2	5.9E-4	-1.3E-4	-5.5E-4	1.1E-4	3.0E-6	-2.6E-6	-3.4E-6	3.1E-6
KJ2 KJ3 KK2 KK3	5.9E-4	-1.2E-4	-5.5E-4	6.2E-5	2.5E-6	-2.1E-6	-2.8E-6	2.3E-6
KJ3 KJ4 KK3 KK4	5.7E-4	-7.7E-5	-5.2E-4	1.8E-5	2.1E-6	-1.8E-6	-2.2E-6	2.0E-6
KJ4 KJ5 KK4 KK5	5.7E-4	-9.8E-5	-5.1E-4	7.6E-5	2.7E-6	-2.4E-6	-3.1E-6	2.8E-6
KJ5 KJ6 KK5 KK6	6.0E-4	-2.0E-4	-5.1E-4	1.1E-4	3.4E-6	-2.8E-6	-4.0E-6	3.4E-6
KJ6 KJ7 KK6 KK7	6.0E-4	-1.7E-4	-4.9E-4	1.0E-4	3.0E-6	-2.6E-6	-3.6E-6	3.3E-6

D Whillans Ice Stream quad strain components

Stations Used	$\dot{\epsilon}_{xx}$	$\dot{\epsilon}_{xy}$	$\dot{\epsilon}_{yx}$	$\dot{\epsilon}_{yy}$	$\dot{\epsilon}_{xx}$ er.	$\dot{\epsilon}_{xy}$ er	$\dot{\epsilon}_{yx}$ er	$\dot{\epsilon}_{yy}$ er
WA1 WB1 WA2 WB2	5.9E-5	1.3E-4	-7.6E-5	4.1E-5	-2.9E-7	9.7E-7	-1.2E-6	9.8E-7
WB1 WC1 WB2 WC2	2.5E-4	1.1E-4	1.9E-4	-9.1E-5	1.5E-6	1.2E-6	1.6E-6	-1.8E-7
WC1 WD1 WC2 WD2	4.3E-4	-6.9E-5	-8.4E-5	-5.7E-5	1.8E-6	-1.1E-7	-9.5E-8	2.7E-8
WD1 WE1 WD2 WE2	6.1E-4	-5.0E-5	1.2E-5	-5.0E-5	1.8E-6	-1.1E-7	5.1E-8	4.8E-8
WE1 WF1* WE2 WF2	NaN	NaN	-3.8E-4	1.2E-4	NaN	NaN	-4.4E-8	-5.5E-7
WF1 WG1* WF2 WG2	NaN	NaN	1.2E-3	-5.4E-5	NaN	NaN	1.3E-6	-4.1E-7
WG1 WH1* WG2 WH2	NaN	NaN	2.9E-4	-4.4E-4	NaN	NaN	1.7E-6	-1.4E-6
WH1 WI1* WH2 WI2	NaN	NaN	7.1E-5	-3.0E-4	NaN	NaN	2.3E-6	-2.0E-6
WI1 WJ1 WI2 WJ2	6.6E-4	-1.6E-4	2.6E-4	-2.9E-4	2.4E-6	-1.8E-6	2.2E-6	-2.0E-6
WJ1 WK1 WJ2 WK2	6.4E-4	-6.6E-5	3.6E-4	-2.4E-4	1.7E-6	-1.2E-6	1.8E-6	-1.5E-6
WK1 WL1 WK2 WL2	6.2E-4	-6.1E-5	4.5E-4	-1.8E-4	1.3E-6	-9.9E-7	1.5E-6	-1.2E-6
WA2 WB2 WA3 WB3	1.2E-4	1.1E-5	-7.0E-5	-9.5E-5	9.7E-7	-1.4E-7	-1.1E-6	-1.1E-6
WB2 WC2 WB3 WC3	1.2E-4	-2.2E-5	3.6E-5	-9.0E-5	1.4E-6	-1.1E-6	1.6E-6	-1.3E-6
WC2 WD2 WC3 WD3	3.3E-4	-3.4E-5	6.8E-5	-1.2E-4	2.0E-6	-1.5E-6	2.2E-6	-1.8E-6
WD2 WE2* WD3 WE3	NaN	NaN	-3.2E-4	-2.7E-4	NaN	NaN	-1.9E-6	-1.5E-6
WE2 WF2* WE3 WF3	NaN	NaN	1.7E-4	-2.7E-4	NaN	NaN	1.3E-6	-1.1E-6
WF2 WG2 WF3 WG3	1.5E-4	-1.5E-4	5.6E-4	-2.4E-4	1.3E-6	-1.1E-6	1.6E-6	-1.3E-6
WG2 WH2* WG3 WH3	NaN	NaN	4.1E-4	-3.8E-4	NaN	NaN	1.7E-6	-1.5E-6
WH2 WI2* WH3 WI3	NaN	NaN	2.4E-4	-3.3E-4	NaN	NaN	1.9E-6	-1.9E-6
WI2 WJ2 WI3 WJ3	7.8E-4	-8.5E-5	3.9E-4	-1.9E-4	2.2E-6	5.0E-8	2.0E-6	-1.8E-6

Stations Used	$\dot{\epsilon}_{xx}$	$\dot{\epsilon}_{xy}$	$\dot{\epsilon}_{yx}$	$\dot{\epsilon}_{yy}$	$\dot{\epsilon}_{xx}$ er.	$\dot{\epsilon}_{xy}$ er	$\dot{\epsilon}_{yx}$ er	$\dot{\epsilon}_{yy}$ er
WJ2 WK2 WJ3 WK3	6.5E-4	-1.8E-4	3.9E-4	-1.5E-4	1.5E-6	-1.4E-6	1.5E-6	-1.5E-6
WK2 WL2 WK3 WL3	6.1E-4	-1.6E-4	4.6E-4	-1.7E-4	1.2E-6	-1.1E-6	1.2E-6	-1.3E-6
WA3 WB3 WA4 WB4	1.6E-4	-2.0E-4	-1.2E-4	-6.2E-5	1.6E-6	-1.8E-6	-1.8E-6	-2.0E-6
WB3 WC3* WB4 WC4	NaN	NaN	3.2E-4	3.1E-4	NaN	NaN	1.9E-6	2.6E-7
WC3 WD3* WC4 WD4	NaN	NaN	-1.3E-4	4.8E-4	NaN	NaN	9.0E-7	3.3E-6
WD3 WE3* WD4 WE4	NaN	NaN	-2.6E-4	5.4E-4	NaN	NaN	-1.9E-6	3.3E-6
WE3 WF3* WE4 WF4	NaN	NaN	1.1E-4	5.2E-4	NaN	NaN	-4.4E-7	3.2E-6
WF3 WG3 WF4 WG4	1.6E-4	-2.4E-4	3.4E-4	-2.7E-5	1.7E-6	-2.7E-6	1.9E-6	5.8E-7
WG3 WH3 WG4 WH4	5.5E-4	-2.2E-4	3.2E-4	-2.6E-4	2.1E-6	-2.7E-6	1.9E-6	-2.6E-6
WH3 WI3 WH4 WI4	7.0E-4	-2.2E-4	3.4E-4	-2.8E-4	2.7E-6	-2.8E-6	2.2E-6	-2.7E-6
WI3 WJ3 WI4 WJ4	7.4E-4	-2.2E-4	4.8E-4	-2.2E-4	3.1E-6	-2.5E-6	2.7E-6	-2.3E-6
WJ3 WK3 WJ4 WK4	7.0E-4	-1.7E-4	4.5E-4	-1.2E-4	2.6E-6	-2.1E-6	2.2E-6	-1.9E-6
WK3 WL3 WK4 WL4	6.7E-4	-1.3E-4	4.9E-4	-2.7E-5	2.0E-6	-1.7E-6	1.9E-6	1.3E-8

* Quads containing damaged stations.

E Whillans Ice Stream triangular strain components

Stations Used	$\dot{\epsilon}_{xx}$	$\dot{\epsilon}_{xy}$	$\dot{\epsilon}_{yx}$	$\dot{\epsilon}_{yy}$	$\dot{\epsilon}_{xx}$ er.	$\dot{\epsilon}_{xy}$ er	$\dot{\epsilon}_{yx}$ er	$\dot{\epsilon}_{yy}$ er
WA1 WF1 WB1	1.2E-4	-3.3E-5	-2.3E-5	5.9E-5	2.4E-8	-6.6E-9	-4.5E-9	1.2E-8
WA2 WK1 WJ1	1.6E-4	-2.1E-4	1.4E-5	-1.1E-4	3.2E-8	-4.1E-8	2.7E-9	-2.1E-8
WJ1 WG1 WF1	7.5E-5	-8.0E-5	-1.7E-5	-7.1E-5	1.5E-8	-1.6E-8	-3.5E-9	-1.4E-8
WK1 WG1 WJ1	3.4E-5	-7.5E-5	-2.1E-5	-7.0E-5	6.9E-9	-1.5E-8	-4.3E-9	-1.4E-8
WA2 WL1 WD2	4.3E-4	-4.1E-4	-6.5E-5	1.5E-4	8.5E-8	-8.2E-8	-1.3E-8	2.9E-8
WC2 WD2 WL1	3.7E-4	-1.5E-4	2.1E-5	-2.2E-4	7.3E-8	-3.1E-8	4.2E-9	-4.4E-8
WC4 WD4 WL3	3.3E-4	-3.5E-4	2.0E-4	-3.4E-4	6.6E-8	-7.1E-8	4.0E-8	-6.8E-8
WH3 WG3 WL3	3.6E-4	-3.4E-4	1.1E-4	-3.7E-4	7.2E-8	-6.9E-8	2.1E-8	-7.4E-8
WJ2 WA3 WK2	2.2E-4	-4.1E-4	4.0E-5	-3.8E-4	4.3E-8	-8.1E-8	7.9E-9	-7.6E-8
WK2 WG2 WJ2	3.2E-5	-1.7E-4	9.6E-5	-4.5E-4	6.3E-9	-3.5E-8	1.9E-8	-9.0E-8
WL2 WG2 WK2	-3.3E-5	-2.5E-4	2.2E-4	-3.0E-4	-6.6E-9	-4.9E-8	4.5E-8	-6.0E-8
WJ2 WI2 WD3	3.1E-4	-3.1E-4	-1.2E-4	-4.9E-4	6.2E-8	-6.3E-8	-2.4E-8	-9.9E-8
WD3 WA3 WJ2	2.2E-4	-4.2E-4	3.1E-5	-3.1E-4	4.4E-8	-8.5E-8	6.1E-9	-6.1E-8
WD1 WL2 WB3	1.4E-3	1.2E-3	1.3E-3	1.5E-3	2.7E-7	2.4E-7	2.6E-7	2.9E-7
WL2 WK2 WB3	2.8E-4	-3.5E-4	8.8E-5	-2.6E-4	5.5E-8	-6.9E-8	1.8E-8	-5.2E-8
WB3 WK2 WA3	2.8E-4	-3.4E-4	8.3E-5	-3.3E-4	5.5E-8	-6.8E-8	1.7E-8	-6.6E-8
WI2 WC2 WK3	-4.4E-3	-6.2E-3	1.1E-2	1.4E-2	-8.7E-7	-1.2E-6	2.2E-6	2.7E-6
WC4 WL3 WK3	3.7E-4	-3.5E-4	1.8E-4	-3.4E-4	7.4E-8	-7.1E-8	3.6E-8	-6.9E-8
WK3 WL3 WG3	3.6E-4	-3.5E-4	9.2E-5	-2.7E-4	7.2E-8	-6.9E-8	1.8E-8	-5.4E-8
WH1 WG1 WK1	-3.3E-5	-1.7E-4	-3.7E-5	-9.1E-5	-6.5E-9	-3.4E-8	-7.3E-9	-1.8E-8
WC1 WB1 WF1	9.8E-5	-5.7E-5	-1.0E-4	-1.8E-5	2.0E-8	-1.1E-8	-2.0E-8	-3.6E-9
WF1 WG1 WC1	5.4E-5	-5.8E-5	-7.0E-5	-1.7E-5	1.1E-8	-1.2E-8	-1.4E-8	-3.4E-9

Stations Used	$\dot{\epsilon}_{xx}$	$\dot{\epsilon}_{xy}$	$\dot{\epsilon}_{yx}$	$\dot{\epsilon}_{yy}$	$\dot{\epsilon}_{xx}$ er.	$\dot{\epsilon}_{xy}$ er	$\dot{\epsilon}_{yx}$ er	$\dot{\epsilon}_{yy}$ er
WC1 WH1 WD1	-2.3E-5	-2.0E-4	-9.3E-5	6.5E-5	-4.7E-9	-4.0E-8	-1.9E-8	1.3E-8
WG1 WH1 WC1	-2.2E-5	-1.8E-4	-9.7E-5	-5.9E-5	-4.5E-9	-3.5E-8	-1.9E-8	-1.2E-8
WI1 WL1 WA2	2.6E-4	-3.1E-4	-1.2E-4	1.8E-4	5.2E-8	-6.2E-8	-2.4E-8	3.6E-8
WA2 WJ1 WI1	2.3E-4	-1.3E-4	-5.5E-5	-1.8E-4	4.5E-8	-2.6E-8	-1.1E-8	-3.7E-8
WJ2 WG2 WF2	5.1E-6	-1.7E-4	2.9E-4	-4.9E-4	1.0E-9	-3.4E-8	5.9E-8	-9.8E-8
WG2 WD2 WF2	2.0E-4	-4.0E-4	-5.3E-5	-8.1E-5	4.1E-8	-8.1E-8	-1.1E-8	-1.6E-8
WD2 WC2 WF2	4.0E-4	-1.7E-4	-1.1E-4	-1.5E-4	8.0E-8	-3.4E-8	-2.1E-8	-2.9E-8
WF2 WI2 WJ2	5.8E-6	-1.7E-4	1.9E-4	-6.4E-4	1.2E-9	-3.3E-8	3.7E-8	-1.3E-7
WF2 WC2 WI2	3.8E-4	-9.5E-5	2.1E-5	-6.8E-4	7.6E-8	-1.9E-8	4.2E-9	-1.4E-7
WE2 WD2 WG2	2.0E-4	-3.6E-4	-8.3E-5	9.8E-5	3.9E-8	-7.2E-8	-1.7E-8	2.0E-8
WE2 WH1 WK1	3.3E-4	-1.6E-5	1.0E-5	-7.2E-5	6.6E-8	-3.3E-9	2.1E-9	-1.4E-8
WD1 WH1 WE2	5.6E-4	2.6E-4	5.7E-4	5.8E-4	1.1E-7	5.2E-8	1.1E-7	1.2E-7
WA4 WL3 WD4	2.8E-4	-4.2E-4	2.0E-4	-3.4E-4	5.6E-8	-8.3E-8	4.1E-8	-6.7E-8
WC3 WG3 WH3	3.4E-4	-3.3E-4	1.6E-5	-3.0E-4	6.8E-8	-6.5E-8	3.2E-9	-6.0E-8
WH3 WD3 WC3	3.5E-4	-4.1E-4	1.5E-5	-2.9E-4	7.0E-8	-8.1E-8	3.0E-9	-5.8E-8
WC3 WD3 WI2	3.0E-4	-3.8E-4	-9.4E-5	-2.4E-4	6.0E-8	-7.7E-8	-1.9E-8	-4.8E-8
WI2 WK3 WC3	2.3E-4	-4.7E-4	-1.4E-3	-2.0E-3	4.7E-8	-9.5E-8	-2.8E-7	-3.9E-7
WC3 WK3 WG3	-1.5E-4	-9.2E-4	-6.1E-4	-1.1E-3	-2.9E-8	-1.8E-7	-1.2E-7	-2.1E-7
WA3 WD3 WE3	3.4E-4	-4.5E-4	6.6E-5	-3.1E-4	6.8E-8	-8.9E-8	1.3E-8	-6.3E-8
WE3 WD3 WH3	3.3E-4	-4.3E-4	3.3E-5	-2.7E-4	6.6E-8	-8.6E-8	6.6E-9	-5.4E-8
WL1 WI1 WE1	-3.6E-3	-4.7E-3	1.5E-2	1.8E-2	-7.1E-7	-9.5E-7	3.0E-6	3.5E-6
WE1 WF1 WA1	9.2E-5	1.5E-4	-2.2E-5	5.4E-5	1.8E-8	2.9E-8	-4.4E-9	1.1E-8
WE1 WJ1 WF1	2.0E-4	6.7E-5	4.9E-5	4.5E-6	4.1E-8	1.3E-8	9.7E-9	9.1E-10
WE1 WI1 WJ1	2.4E-4	-1.4E-4	1.0E-4	-2.9E-4	4.9E-8	-2.8E-8	2.1E-8	-5.7E-8

Stations Used	$\dot{\epsilon}_{xx}$	$\dot{\epsilon}_{xy}$	$\dot{\epsilon}_{yx}$	$\dot{\epsilon}_{yy}$	$\dot{\epsilon}_{xx}$ er.	$\dot{\epsilon}_{xy}$ er	$\dot{\epsilon}_{yx}$ er	$\dot{\epsilon}_{yy}$ er
WH2 WG2 WL2	-2.8E-5	-2.1E-4	2.8E-4	1.3E-4	-5.7E-9	-4.2E-8	5.6E-8	2.6E-8
WH2 WE2 WG2	3.4E-4	-2.7E-4	3.3E-5	1.7E-4	6.8E-8	-5.4E-8	6.6E-9	3.4E-8
WH2 WL2 WD1	-9.5E-4	-1.4E-3	1.1E-3	1.2E-3	-1.9E-7	-2.9E-7	2.1E-7	2.3E-7
WD1 WE2 WH2	1.8E-3	1.5E-3	-7.2E-4	-7.8E-4	3.6E-7	3.1E-7	-1.4E-7	-1.6E-7
WA2 WD2 WB2	3.9E-4	-4.5E-4	-1.6E-4	2.4E-5	7.9E-8	-9.0E-8	-3.1E-8	4.9E-9
WD2 WE2 WB2	2.9E-4	-4.3E-4	5.0E-5	-1.2E-5	5.7E-8	-8.6E-8	1.0E-8	-2.4E-9
WB2 WK1 WA2	1.7E-4	-2.1E-4	-4.2E-5	-9.8E-5	3.3E-8	-4.1E-8	-8.5E-9	-2.0E-8
WB2 WE2 WK1	3.6E-4	6.4E-5	5.9E-5	4.0E-5	7.3E-8	1.3E-8	1.2E-8	8.0E-9
WE4 WD4 WF4	9.3E-4	-9.0E-4	3.9E-3	-3.3E-3	1.9E-7	-1.8E-7	7.9E-7	-6.7E-7
WE4 WA4 WD4	3.2E-4	-4.1E-4	2.0E-4	-3.4E-4	6.4E-8	-8.2E-8	4.0E-8	-6.7E-8
WF4 WB4 WE4	3.5E-4	-4.1E-4	3.1E-4	-2.6E-4	7.1E-8	-8.2E-8	6.2E-8	-5.2E-8
WE4 WB4 WA4	3.2E-4	-4.1E-4	2.5E-4	-2.7E-4	6.4E-8	-8.3E-8	5.0E-8	-5.3E-8
WF3 WB3 WA3	3.5E-4	-3.8E-4	7.4E-5	-3.2E-4	7.1E-8	-7.6E-8	1.5E-8	-6.5E-8
WA3 WE3 WF3	3.5E-4	-4.3E-4	7.4E-5	-3.1E-4	7.1E-8	-8.7E-8	1.5E-8	-6.1E-8
WF3 WE3 WJ3	2.8E-4	-3.9E-4	1.4E-4	-3.4E-4	5.6E-8	-7.9E-8	2.7E-8	-6.8E-8
WD1 WB3 WF3	1.9E-3	1.8E-3	1.5E-3	1.6E-3	3.8E-7	3.7E-7	2.9E-7	3.2E-7
WJ3 WB4 WF3	4.4E-3	4.3E-3	3.5E-3	3.6E-3	8.7E-7	8.6E-7	7.1E-7	7.2E-7
WI3 WE3 WH3	2.8E-4	-4.3E-4	1.5E-4	-2.7E-4	5.6E-8	-8.6E-8	3.0E-8	-5.5E-8
WH3 WL3 WI3	2.9E-4	-4.4E-4	1.7E-4	-2.9E-4	5.8E-8	-8.8E-8	3.3E-8	-5.8E-8
WL3 WA4 WI3	3.0E-4	-4.4E-4	1.5E-4	-2.9E-4	6.1E-8	-8.8E-8	3.0E-8	-5.8E-8
WJ3 WE3 WI3	2.8E-4	-4.3E-4	1.4E-4	-2.9E-4	5.6E-8	-8.6E-8	2.7E-8	-5.7E-8
WI3 WB4 WJ3	3.3E-4	-4.7E-4	2.1E-4	-3.5E-4	6.5E-8	-9.3E-8	4.3E-8	-7.0E-8
WA4 WB4 WI3	3.2E-4	-4.2E-4	2.0E-4	-2.3E-4	6.4E-8	-8.3E-8	4.1E-8	-4.6E-8

F Kamb Ice Stream principle strains

Stations Used	principle strain rate 1	principle strain rate 1 e	principle strain rate 2	principle strain rate 2 e
KA1 KA2 KB1 KB2	-4.9E-5	-1.4E-4	6.1E-5	-1.4E-4
KA2 KA3 KB2 KB3	-7.3E-5	-1.3E-4	2.2E-4	-1.3E-4
KA3 KA4 KB3 KB4	-2.0E-3	-1.3E-4	1.2E-3	-1.3E-4
KA4 KA5 KB4 KB5	-1.8E-4	8.8E-5	1.2E-3	8.8E-5
KA5 KA6 KB5 KB6	-1.0E-3	-1.6E-5	3.1E-3	-1.6E-5
KA6 KA7 KB6 KB7	-1.6E-4	3.5E-4	8.3E-4	3.5E-4
KB1 KB2 KC1 KC2	-1.3E-4	7.8E-4	8.6E-4	7.8E-4
KB2 KB3 KC2 KC3	-9.3E-5	8.6E-4	8.6E-4	8.6E-4
KB3 KB4 KC3 KC4	-8.4E-5	7.3E-4	8.3E-4	7.3E-4
KB4 KB5 KC4 KC5	-6.9E-5	6.1E-4	7.6E-4	6.1E-4
KB5 KB6 KC5 KC6	-1.3E-5	-5.4E-5	5.9E-5	-5.4E-5
KB6 KB7 KC6 KC7	-3.7E-5	-1.9E-5	2.0E-4	-1.9E-5
KC1 KC2 KD1 KD2	-6.5E-5	5.1E-5	4.8E-4	5.1E-5
KC2 KC3 KD2 KD3	-3.4E-3	-1.1E-3	6.0E-6	-1.1E-3
KC3 KC4 KD3 KD4	-3.9E-4	2.1E-4	5.8E-3	2.1E-4
KC4 KC5 KD4 KD5	-1.5E-4	3.2E-4	9.8E-4	3.2E-4
KC5 KC6 KD5 KD6	-1.2E-4	7.5E-4	8.9E-4	7.5E-4
KC6 KC7 KD6 KD7	-8.4E-5	7.0E-4	9.3E-4	7.0E-4
KD1 KD2 KE1 KE2	-9.0E-5	5.3E-4	8.2E-4	5.3E-4
KD2 KD3 KE2 KE3	-1.0E-4	4.8E-4	7.5E-4	4.8E-4

Stations Used	principle strain rate 1	principle strain rate 1 e	principle strain rate 2	principle strain rate 2 e
KD3 KD4 KE3 KE4	6.8E-6	3.2E-4	7.9E-5	3.2E-4
KD4 KD5 KE4 KE5	-2.6E-6	7.4E-4	1.7E-4	7.4E-4
KD5 KD6 KE5 KE6	-3.4E-5	4.3E-4	3.9E-4	4.3E-4
KD6 KD7 KE6 KE7	-1.5E-3	7.9E-6	9.8E-4	8.0E-6
KE1 KE2 KF1 KF2	-4.7E-4	5.0E-4	4.3E-3	5.0E-4
KE2 KE3 KF2 KF3	-2.2E-4	3.0E-4	1.2E-3	3.0E-4
KE3 KE4 KF3 KF4	-1.8E-4	6.1E-4	8.3E-4	6.1E-4
KE4 KE5 KF4 KF5	-1.2E-4	7.1E-4	9.1E-4	7.1E-4
KE5 KE6 KF5 KF6	-1.0E-4	6.8E-4	7.8E-4	6.8E-4
KE6 KE7 KF6 KF7	-1.1E-4	4.0E-4	7.0E-4	4.0E-4
KF1 KF2 KG1 KG2	1.9E-5	5.2E-4	8.7E-5	5.2E-4
KF2 KF3 KG2 KG3	2.4E-5	6.9E-4	1.6E-4	6.9E-4
KF3 KF4 KG3 KG4	5.2E-5	8.2E-4	3.4E-4	8.2E-4
KF4 KF5 KG4 KG5	1.2E-4	9.3E-4	9.5E-4	9.3E-4
KF5 KF6 KG5 KG6	-1.1E-4	5.7E-4	1.4E-3	5.7E-4
KF6 KF7 KG6 KG7	-1.4E-4	5.5E-4	1.5E-3	5.5E-4
KG1 KG2 KH1 KH2	-1.1E-4	5.8E-4	8.8E-4	5.8E-4
KG2 KG3 KH2 KH3	-9.5E-5	6.1E-4	9.4E-4	6.1E-4
KG3 KG4 KH3 KH4	-7.1E-5	7.5E-4	7.6E-4	7.5E-4
KG4 KG5 KH4 KH5	-6.7E-5	5.6E-4	7.2E-4	5.6E-4
KG5 KG6 KH5 KH6	-1.1E-5	7.9E-4	1.2E-4	7.9E-4

Stations Used	principle strain rate 1	principle strain rate 1 e	principle strain rate 2	principle strain rate 2 e
KG6 KG7 KH6 KH7	2.1E-5	8.3E-4	2.1E-4	8.3E-4
KH1 KH2 KI1 KI2	3.1E-5	1.0E-3	4.8E-4	1.0E-3
KH2 KH3 KI2 KI3	8.4E-5	1.0E-3	1.1E-3	1.0E-3
KH3 KH4 KI3 KI4	1.5E-5	7.2E-4	1.4E-3	7.1E-4
KH4 KH5 KI4 KI5	-1.0E-4	6.7E-4	1.4E-3	6.7E-4
KH5 KH6 KI5 KI6	-9.0E-5	6.4E-4	8.6E-4	6.4E-4
KH6 KH7 KI6 KI7	-8.7E-5	5.5E-4	9.7E-4	5.5E-4
KI1 KI2 KJ1 KJ2	-6.9E-5	6.2E-4	8.0E-4	6.2E-4
KI2 KI3 KJ2 KJ3	-7.6E-5	6.8E-4	7.8E-4	6.8E-4
KI3 KI4 KJ3 KJ4	-8.7E-4	8.4E-4	2.6E-3	8.4E-4
KI4 KI5 KJ4 KJ5	-2.9E-3	-3.8E-4	9.6E-5	-3.8E-4
KI5 KI6 KJ5 KJ6	-5.4E-4	1.0E-3	2.6E-3	1.0E-3
KI6 KI7 KJ6 KJ7	4.1E-5	1.3E-3	1.3E-3	1.2E-3
KJ1 KJ2 KK1 KK2	6.9E-5	8.2E-4	1.5E-3	8.2E-4
KJ2 KJ3 KK2 KK3	1.5E-5	5.0E-4	1.4E-3	5.0E-4
KJ3 KJ4 KK3 KK4	-2.7E-5	4.9E-4	9.4E-4	4.9E-4
KJ4 KJ5 KK4 KK5	-6.1E-5	5.4E-4	1.1E-3	5.4E-4
KJ5 KJ6 KK5 KK6	-6.1E-5	6.1E-4	8.4E-4	6.1E-4
KJ6 KJ7 KK6 KK7	-6.0E-5	6.4E-4	7.6E-4	6.3E-4

G Whillans Ice Stream quad principle strains

Stations Used	principle strain rate 1	principle strain rate 1 e	principle strain rate 2	principle strain rate 2 e
WA1 WB1				
WA2 WB2	2.1E-5	6.9E-7	7.8E-5	6.9E-7
WB1 WC1				
WB2 WC2	-1.5E-4	1.3E-6	3.1E-4	1.3E-6
WC1 WD1				
WC2 WD2	-6.8E-5	1.8E-6	4.4E-4	1.8E-6
WD1 WE1				
WD2 WE2	-5.0E-5	1.9E-6	6.1E-4	1.9E-6
WE1 WF1*				
WE2 WF2	NaN	0.0E+0	NaN	0.0E+0
WF1 WG1*				
WF2 WG2	NaN	0.0E+0	NaN	0.0E+0
WG1 WH1*				
WG2 WH2	NaN	0.0E+0	NaN	0.0E+0
WH1 WI1*				
WH2 WI2	NaN	0.0E+0	NaN	0.0E+0
WI1 WJ1				
WI2 WJ2	-2.9E-4	3.8E-7	6.6E-4	3.8E-7
WJ1 WK1				
WJ2 WK2	-2.7E-4	1.2E-7	6.7E-4	1.2E-7
WA2 WB2				
WA3 WB3	-9.9E-5	-1.0E-7	1.3E-4	-1.0E-7
WB2 WC2				
WB3 WC3	-9.0E-5	6.8E-8	1.2E-4	6.8E-8
WC2 WD2				
WC3 WD3	-1.2E-4	1.6E-7	3.3E-4	1.6E-7
WD2 WE2*				
WD3 WE3	NaN	0.0E+0	NaN	0.0E+0
WE2 WF2*				
WE3 WF3	NaN	0.0E+0	NaN	0.0E+0
WF2 WG2				
WF3 WG3	-3.3E-4	4.4E-8	2.4E-4	4.4E-8
WG2 WH2*				
WG3 WH3	NaN	0.0E+0	NaN	0.0E+0
WH2 WI2*				
WH3 WI3	NaN	0.0E+0	NaN	0.0E+0
WI2 WJ2				
WI3 WJ3	-2.1E-4	3.7E-7	8.0E-4	3.7E-7
WJ2 WK2				
WJ3 WK3	-1.6E-4	-2.2E-8	6.6E-4	-2.2E-8
WA3 WB3				
WA4 WB4	-1.5E-4	-4.3E-7	2.5E-4	-4.3E-7
WB3 WC3*				
WB4 WC4	NaN	0.0E+0	NaN	0.0E+0

Stations Used	principle strain rate 1	principle strain rate 1 e	principle strain rate 2	principle strain rate 2 e
WC3 WD3*				
WC4 WD4	NaN	0.0E+0	NaN	0.0E+0
WD3 WE3*				
WD4 WE4	NaN	0.0E+0	NaN	0.0E+0
WE3 WF3*				
WE4 WF4	NaN	0.0E+0	NaN	0.0E+0
WF3 WG3				
WF4 WG4	-3.9E-5	2.3E-6	1.7E-4	2.3E-6
WG3 WH3				
WG4 WH4	-2.6E-4	-5.2E-7	5.5E-4	-5.2E-7
WH3 WI3				
WH4 WI4	-2.8E-4	2.9E-8	7.1E-4	2.9E-8
WI3 WJ3				
WI4 WJ4	-2.4E-4	8.6E-7	7.6E-4	8.6E-7
WJ3 WK3				
WJ4 WK4	-1.4E-4	6.3E-7	7.2E-4	6.3E-7
WK3 WL3				
WK4 WL4	-7.1E-5	2.0E-6	7.1E-4	2.0E-6

* Quads containing damaged stations.

H Whillans Ice Stream triangular principle strains

Stations Used	principle strain rate 1	principle strain rate 1 er.	principle strain rate 2	principle strain rate 2 er.
WA1 WF1 WB1	4.8E-5	1.0E-7	1.3E-4	2.8E-7
WA2 WK1 WJ1	-1.4E-4	-2.9E-7	1.9E-4	4.0E-7
WJ1 WG1 WF1	-8.5E-5	-1.8E-7	8.9E-5	1.9E-7
WK1 WG1 WJ1	-8.9E-5	-1.9E-7	5.3E-5	1.1E-7
WA2 WL1 WD2	9.9E-6	2.1E-8	5.6E-4	1.2E-6
WC2 WD2 WL1	-2.3E-4	-4.7E-7	3.7E-4	7.8E-7
WC4 WD4 WL3	-3.5E-4	-7.4E-7	3.4E-4	7.1E-7
WH3 WG3 WL3	-3.9E-4	-8.1E-7	3.8E-4	8.0E-7
WJ2 WA3 WK2	-4.3E-4	-9.0E-7	2.7E-4	5.7E-7
WK2 WG2 WJ2	-4.5E-4	-9.5E-7	3.5E-5	7.3E-8
WL2 WG2 WK2	-3.0E-4	-6.4E-7	-3.2E-5	-6.8E-8
WJ2 WI2 WD3	-5.5E-4	-1.2E-6	3.6E-4	7.6E-7
WD3 WA3 WJ2	-3.7E-4	-7.8E-7	2.9E-4	6.0E-7
WD1 WL2 WB3	1.6E-4	3.4E-7	2.7E-3	5.6E-6
WL2 WK2 WB3	-2.9E-4	-6.0E-7	3.1E-4	6.4E-7
WB3 WK2 WA3	-3.6E-4	-7.5E-7	3.0E-4	6.3E-7
WI2 WC2 WK3	-4.7E-3	-9.9E-6	1.4E-2	2.9E-5
WC4 WL3 WK3	-3.5E-4	-7.4E-7	3.8E-4	8.0E-7
WK3 WL3 WG3	-3.0E-4	-6.2E-7	3.9E-4	8.1E-7
WH1 WG1 WK1	-1.7E-4	-3.6E-7	4.5E-5	9.5E-8
WC1 WB1 WF1	-5.7E-5	-1.2E-7	1.4E-4	2.9E-7
WF1 WG1 WC1	-5.5E-5	-1.2E-7	9.2E-5	1.9E-7
WC1 WH1	-1.3E-4	-2.8E-7	1.7E-4	3.7E-7

Stations Used	principle strain rate 1	principle strain rate 1 er.	principle strain rate 2	principle strain rate 2 er.
WD1 WG1 WH1 WC1	-1.8E-4	-3.7E-7	9.7E-5	2.0E-7
WI1 WL1 WA2	-1.4E-7	-3.0E-10	4.4E-4	9.2E-7
WA2 WJ1 WI1	-2.0E-4	-4.3E-7	2.5E-4	5.2E-7
WJ2 WG2 WF2	-5.0E-4	-1.0E-6	1.3E-5	2.7E-8
WG2 WD2 WF2	-2.1E-4	-4.4E-7	3.3E-4	7.0E-7
WD2 WC2 WF2	-1.8E-4	-3.8E-7	4.3E-4	9.1E-7
WF2 WI2 WJ2	-6.4E-4	-1.4E-6	5.9E-6	1.2E-8
WF2 WC2 WI2	-6.8E-4	-1.4E-6	3.8E-4	8.0E-7
WE2 WD2 WG2	-7.9E-5	-1.7E-7	3.7E-4	7.9E-7
WE2 WH1 WK1	-7.2E-5	-1.5E-7	3.3E-4	6.9E-7
WD1 WH1 WE2	1.6E-4	3.3E-7	9.9E-4	2.1E-6
WA4 WL3 WD4	-3.5E-4	-7.4E-7	3.0E-4	6.3E-7
WC3 WG3 WH3	-3.4E-4	-7.1E-7	3.8E-4	7.9E-7
WH3 WD3 WC3	-3.4E-4	-7.2E-7	4.1E-4	8.5E-7
WC3 WD3 WI2	-3.3E-4	-6.9E-7	3.9E-4	8.2E-7
WI2 WK3 WC3	-2.3E-3	-4.9E-6	5.8E-4	1.2E-6
WC3 WK3 WG3	-1.5E-3	-3.1E-6	2.9E-4	6.0E-7
WA3 WD3 WE3	-3.7E-4	-7.7E-7	3.9E-4	8.2E-7
WE3 WD3 WH3	-3.3E-4	-6.9E-7	3.9E-4	8.2E-7
WL1 WI1 WE1	-4.7E-3	-9.9E-6	1.9E-2	3.9E-5
WE1 WF1 WA1	8.8E-6	1.8E-8	1.4E-4	2.9E-7
WE1 WJ1 WF1	-1.1E-5	-2.3E-8	2.2E-4	4.6E-7
WE1 WI1 WJ1	-2.9E-4	-6.0E-7	2.4E-4	5.1E-7
WH2 WG2	-3.6E-5	-7.5E-8	1.4E-4	2.9E-7

Stations Used	principle strain rate 1	principle strain rate 1 er.	principle strain rate 2	principle strain rate 2 er.
WL2 WH2 WE2 WG2	1.1E-4	2.3E-7	4.0E-4	8.4E-7
WH2 WL2 WD1	-9.7E-4	-2.0E-6	1.2E-3	2.5E-6
WD1 WE2 WH2	-8.4E-4	-1.8E-6	1.8E-3	3.9E-6
WA2 WD2 WB2	-1.5E-4	-3.1E-7	5.6E-4	1.2E-6
WD2 WE2 WB2	-1.1E-4	-2.2E-7	3.8E-4	7.9E-7
WB2 WK1 WA2	-1.5E-4	-3.1E-7	2.1E-4	4.5E-7
WB2 WE2 WK1	2.9E-5	6.0E-8	3.7E-4	7.9E-7
WE4 WD4 WF4	-3.8E-3	-8.0E-6	1.4E-3	3.0E-6
WE4 WA4 WD4	-3.5E-4	-7.4E-7	3.4E-4	7.1E-7
WF4 WB4 WE4	-2.6E-4	-5.5E-7	3.6E-4	7.5E-7
WE4 WB4 WA4	-2.8E-4	-5.8E-7	3.3E-4	6.9E-7
WF3 WB3 WA3	-3.6E-4	-7.5E-7	3.9E-4	8.1E-7
WA3 WE3 WF3	-3.5E-4	-7.4E-7	4.0E-4	8.4E-7
WF3 WE3 WJ3	-3.6E-4	-7.7E-7	3.1E-4	6.4E-7
WD1 WB3 WF3	1.2E-4	2.6E-7	3.4E-3	7.2E-6
WJ3 WB4 WF3	3.0E-5	6.4E-8	7.9E-3	1.7E-5
WI3 WE3 WH3	-3.1E-4	-6.5E-7	3.1E-4	6.5E-7
WH3 WL3 WI3	-3.2E-4	-6.7E-7	3.2E-4	6.7E-7
WL3 WA4 WI3	-3.2E-4	-6.8E-7	3.4E-4	7.1E-7
WJ3 WE3 WI3	-3.2E-4	-6.8E-7	3.2E-4	6.6E-7
WI3 WB4 WJ3	-3.7E-4	-7.8E-7	3.5E-4	7.3E-7
WA4 WB4 WI3	-2.5E-4	-5.2E-7	3.4E-4	7.2E-7